

# HD 34736: An intensely magnetised double-lined spectroscopic binary with rapidly-rotating chemically peculiar B-type components

E. Semenko,<sup>1\*</sup> O. Kochukhov,<sup>2</sup> Z. Mikulášek,<sup>3</sup> G. A. Wade,<sup>4</sup> E. Alecian,<sup>5</sup> D. Bohlender,<sup>6</sup> B. Das,<sup>7</sup> D. L. Feliz,<sup>8</sup> J. Janík,<sup>3</sup> J. Kolář,<sup>3</sup> J. Krtička,<sup>3</sup> D. O. Kudryavtsev,<sup>9</sup> J. M. Labadie-Bartz,<sup>10</sup> D. Mkrtichian,<sup>1</sup> D. Monin,<sup>6</sup> V. Petit,<sup>11</sup> I. I. Romanyuk,<sup>9</sup> M. E. Shultz,<sup>11</sup> D. Shulyak,<sup>12</sup> R. J. Siverd,<sup>13</sup> A. Tkachenko,<sup>14</sup> I. A. Yakunin,<sup>9,15</sup> M. Zejda,<sup>3</sup> and the BinaMiCS collaboration

<sup>1</sup>National Astronomical Research Institute of Thailand, 260 Moo 4, T. Donkaew, A. Maerim, 50180, Chiangmai, Thailand

<sup>2</sup>Department of Physics and Astronomy, Uppsala University, Box 516, 75120 Uppsala, Sweden

<sup>3</sup>Department of Theoretical Physics and Astrophysics, Masaryk University, Kotlářská 2, CZ 611 37 Brno, Czech Republic

<sup>4</sup>Department of Physics & Space Science, Royal Military College of Canada, PO Box 17000 Station Forces, Kingston, ON, Canada K7K 0C6

<sup>5</sup>Université Grenoble Alpes, IPAG, F-38000 Grenoble, France

<sup>6</sup>National Research Council of Canada, Herzberg Astronomy and Astrophysics Research Centre, 5071 West Saanich Road, Victoria, BC V9E 2E7, Canada

<sup>7</sup>CSIRO, Space and Astronomy, P.O. Box 1130, Bentley WA 6102, Australia

<sup>8</sup>American Museum of Natural History, 200 Central Park West, Manhattan, NY 10024, USA

<sup>9</sup>Special Astrophysical Observatory, Russian Academy of Sciences, Nizhnii Arkhyz, Russia, 369167

<sup>10</sup>LESIA, Paris Observatory, PSL University, CNRS, Sorbonne University, Université Paris Cité, 5 place Jules Janssen, 92195 Meudon, France

<sup>11</sup>Dept. of Physics and Astronomy & Bartol Research Institute, University of Delaware, Newark, DE, 19716, USA

<sup>12</sup>Instituto de Astrofísica de Andalucía - CSIC, c/ Glorieta de la Astronomía s/n, 18008 Granada, Spain

<sup>13</sup>Institute for Astronomy, University of Hawaii, 2680 Woodlawn, Honolulu, HI 96822, USA

<sup>14</sup>Institute of Astronomy, KU Leuven, Celestijnenlaan 200D, 3001 Leuven, Belgium

<sup>15</sup>Saint Petersburg State University, Saint Petersburg 199034, Russia

Accepted XXX. Received YYY; in original form ZZZ

## ABSTRACT

We report the results of a comprehensive study of the spectroscopic binary (SB2) system HD 34736 hosting two chemically peculiar (CP) late B-type stars. Using new and archival observational data, we characterise the system and its components, including their rotation and magnetic fields. Fitting of the radial velocities yields  $P_{\text{orb}} = 83^{\text{d}}219(3)$  and  $e = 0.8103(3)$ . The primary component is a CP He-wk star with  $T_{\text{effA}} = 13000 \pm 500$  K and  $v_e \sin i = 75 \pm 3$  km s<sup>-1</sup>, while the secondary exhibits variability of Mg and Si lines, and has  $T_{\text{effB}} = 11500 \pm 1000$  K and  $v_e \sin i = 110\text{--}180$  km s<sup>-1</sup>. TESS and KELT photometry reveal clear variability of the primary component with a rotational period  $P_{\text{rotA}} = 1^{\text{d}}279\,988\,5(11)$ , which is lengthening at a rate of  $1.26(6)$  s yr<sup>-1</sup>. For the secondary,  $P_{\text{rotB}} = 0^{\text{d}}522\,693\,8(5)$ , reducing at a rate of  $-0.14(3)$  s yr<sup>-1</sup>. The longitudinal component  $\langle B_z \rangle$  of the primary's strongly asymmetric global magnetic field varies from  $-6$  to  $+5$  kG. Weak spectropolarimetric evidence of a magnetic field is found for the secondary star. The observed X-ray and radio emission of HD 34736 may equally be linked to a suspected T Tau-like companion or magnetospheric emission from the principal components. Given the presence of a possible third magnetically active body, one can propose that the magnetic characteristics of the protostellar environment may be connected to the formation of such systems.

**Key words:** stars: magnetic field – stars: chemically peculiar – stars: binaries: spectroscopic – techniques: polarimetric

## 1 INTRODUCTION

Chemically Peculiar, or CP, stars comprise an important group of upper main sequence objects. The catalogue compiled by [Renson & Manfroid \(2009\)](#) lists 8205 known or suspected CP stars in the range of effective temperatures between approximately 7 and 25 kK. Among them, 3652 stars exhibit abnormal lines of helium, iron-peak elements, and rare-earth elements in their spectra. Such stars are

commonly referred to as Ap/Bp or CP2 stars. The latter designation, introduced by [Preston \(1974\)](#), is often applied to early-type variable stars with stable magnetic fields, which generally have globally organized (approximately simple dipolar or low-order multipolar) configurations. While these magnetic fields have only been observationally detected in 10–15% of CP2 stars, all such stars are believed to be magnetic ([Shorlin et al. 2002](#)).

The spectral peculiarities of CP2 stars are understood to be a superficial effect resulting from atomic diffusion enabled by their magnetic fields and generally slow rotation. On a relatively short

\* E-mail: eugene@narit.or.th

timescale, the diffusion process produces abnormal vertical and surface distributions of select chemical elements, resulting in a typical (although quite diverse) spectrum of peculiarities (Kochukhov 2018). The presence of regions of chemical contrast in stellar photospheres (sometimes referred to as “chemical spots”) produce rotationally modulated photometric variability due to flux redistribution. The modern theory of atomic diffusion, developed from the early foundation by Michaud (1970), can explain a wide range of chemical anomalies observed in upper main sequence stars (Michaud et al. 2015).

The CP2 phenomenon first appears in main sequence stars with masses  $\sim 1.4 M_{\odot}$ , with an incidence rapidly increasing to 10–15% for masses of  $3.6 M_{\odot}$  (e.g., Sikora et al. 2019a). However, there is no direct correlation between the mass and the strength of the measured magnetic field (e.g., Shultz et al. 2019b). Fields up to several tens of kG are not particularly rare, even in quite cool Ap stars (e.g., HD 154708 – Hubrig et al. (2005), HD 178892 – Ryabchikova et al. (2006)). A lower field limit of around 100–300 G (the so-called “magnetic desert”, Aurière et al. 2007; Lignières et al. 2014; Kochukhov et al. 2023) probably has a physical meaning. Theoretical studies link the existence of this lower field limit in CP2 stars to specific processes of early stellar formation (e.g., Jermyn & Cantiello 2020; Jouve et al. 2020; Monteiro et al. 2023). While the properties of fossil magnetic fields are well known, the origin of magnetism in peculiar stars remains unclear.

The evolutionary decay of magnetic field strengths, found, for example, by Landstreet et al. (2007); Sikora et al. (2019b) and Shultz et al. (2019b), suggests that among various hypotheses proposed to explain the phenomenon of magnetic CP2 stars, the most plausible is that of a fossil origin. This hypothesis states that the field observed on the main sequence descends from a seed field acquired during the earlier stages of stellar evolution. The seed can be a local galactic magnetic field in the region of formation of the star (Moss 1989), amplified through turbulent processes such as a pre-main sequence dynamo or stellar mass transfer or mergers (Schneider et al. 2019). The latter scenario might explain the observed low incidence of CP2 stars in short-period binary and multiple systems (Alecian et al. 2015).

An observational survey aimed at studying the formation and evolution of magnetic fields in CP2 stars of the Orion OB1 stellar association was initiated at the Special Astrophysical Observatory of the Russian Academy of Sciences (SAO) in 2013 (Romanyuk et al. 2013). In the survey, special attention was paid to the completeness of the sample. Individual measurements of the longitudinal magnetic field  $\langle B_z \rangle$ , i.e. the magnetic field projected to the line of sight and averaged over the visible stellar hemisphere, were obtained using the Main Stellar Spectrograph (MSS) of the 6-m Big Telescope Altazimuthal (BTA) installed in the North Caucasus mountains and then published in a series of papers by Romanyuk et al. (2019, 2021a,b). In 2022, when the observational component of the survey was completed, Semenko et al. (2022) summarised the results. Altogether, 31 CP2 stars out of 56 were found or confirmed as magnetic. For 14 stars, this status was established for the first time. All programme stars were observed at least four times to avoid potential non-detection due to the rotational variation of the field.

As a member of Orion OB1, HD 34736, was selected for spectropolarimetric observation among the other CP2 stars of subgroup 1c (corresponding to an age  $\log t = 6.66$ , Brown et al. 1994) of the association. The signatures of a strong, variable magnetic field were detected in the first spectra of HD 34736 from 2013. The star showed an extraordinarily strong magnetic field  $\langle B_z \rangle$  exceeding 5 kG. Moreover, the star was recognized as an SB2 system consisting of two

early-type stars. The magnetic field was detected only in the dominant spectrum of the narrow-lined component, which we refer to hereafter as the magnetic primary. A short period  $P = 0^d.3603$  extracted from the *HIPPARCOS* photometry was tentatively considered as the possible period of orbital motion in the system. These results were published by Semenko et al. (2014), or Paper I hereinafter. The true period of magnetic field variations,  $P = 1^d.29$ , identified with the rotational period of the primary component, was announced later by Romanyuk et al. (2017).

A strong magnetic field and the suspected short orbital period made HD 34736 a fascinating system for detailed study within the framework of the Binarity and Magnetic Interactions in Stars (BinaMICS) project (Alecian et al. 2015). Compact binaries with magnetic CP components are important laboratories to understanding the origin and evolution of stellar magnetic fields in the upper main sequence.

Here, we present the results of a comprehensive study of HD 34736 carried out within the BinaMICS project. The rest of this paper is organized as follows: In Section 2, we describe the observational material obtained for this study and its processing. Data analysis and results are presented in Section 3. Section 4 summarises the findings and presents the discussion.

## 2 OBSERVATIONS

For this study, we organised a multi-site spectroscopic and spectropolarimetric monitoring campaign with observational facilities in Europe, Asia, and North America. The observation times are summarised in Table 1. Photometric variability of the star was studied using archival photometry from ground and space telescopes. The subsequent sections explain the details of data acquisition and processing.

### 2.1 Spectroscopy and spectropolarimetry

#### 2.1.1 Medium-resolution spectropolarimetry at SAO and DAO

During the period 2013–2020, HD 34736 was observed 137 times with the Main Stellar Spectrograph (MSS, Panchuk et al. 2014) of the 6-m telescope at the Special Astrophysical Observatory (SAO) in the North Caucasian region of Russia. An individual observation consisted of two sub-exposures, normally limited to 10 min. In this case, the mean signal-to-noise ratio of combined spectra measured at 455 nm varied between 200 and 300 depending on the observational conditions. The data handling and techniques used for the longitudinal magnetic field measurement are described in detail by Semenko et al. (2022).

Ten medium-resolution spectropolarimetric observations were obtained with dimaPol ( $R \approx 10\,000$ ) installed at the Dominion Astrophysical Observatory (DAO) from Nov. 10 2014 to Mar. 6 2015. The Stokes  $V$  observations of the  $H_{\beta}$  line were used to derive longitudinal field measurements (Monin et al. 2012); the Heliocentric Julian Days and corresponding longitudinal field measurements are listed in Table 1.

#### 2.1.2 ESPaDOoS spectropolarimetry

An Echelle SpectroPolarimetric Device for the Observation of Stars (ESPaDOoS) (Donati 2003) is a fibre-fed high-resolution ( $R \approx 65\,000$ ) échelle spectrograph, equipped with a polarimeter

placed at the Cassegrain focus of the Canada-France-Hawaii Telescope (CFHT). ESPaDOnS observations were obtained in 2014–2016 over two runs separated by one year within the context of the BinaMICS Large Program (Alecian et al. 2015). The 2014–2015 run was aimed at detecting magnetic fields and following them over the rotational and orbital periods of the system. The second run, scheduled in January 2016, was aimed at dense observations around periastron, where the radial velocity separation of the components is greatest, but also where both components are physically the closest, hence, when maximum interactions (e.g. tidal or electromagnetic) may occur. In total, 22 circularly polarised (Stokes  $I$  and  $V$ ) spectra have been obtained over a little more than 1 year. Individual observations are separated by several hours to several days or weeks, depending on the run (see the log of the observations in Table 1). Each polarimetric spectrum has been obtained by combining 4 successive sub-exposures of 780 s, between which the Fresnel rhombs were rotated by  $90^\circ$ . The total exposure time of each ESPaDOnS observation was 3120 s. The data have been reduced at the CFHT using the UPENA pipeline feeding the LIBRE-ESPRIT package (Donati et al. 1997). The peak signal-to-noise ratio of the polarised spectra ranges from 420 to 600 depending on the observing conditions.

### 2.1.3 Medium- and high-resolution spectroscopy

Four spectra of HD 34736 were collected with the Medium Resolution Echelle Spectrograph (MRES) of the 2.4 m Thai National Telescope at Doi Inthanon (Chiang Mai, Thailand) in 2016 and 2021. MRES is a fibre-fed échelle spectrograph designed to register spectra from 420 to 900 nm with resolving power  $R = 16\,000$ – $20\,000$  depending on three available modes. This spectrograph is installed in a room with thermal control and is well suited to accurate measurement of radial velocities. One-dimensional spectra were extracted from the CCD frames in a standard way using the Image Reduction and Analysis Facility (IRAF). A Th-Ar lamp was used to calibrate spectra in the wavelength domain. Resulting spectra with  $S/N = 80$ – $170$  at 550 nm were cropped to 440–700 nm and normalized to the continuum.

Sixteen high-resolution spectra were obtained with the High Efficiency and Resolution Mercator Echelle Spectrograph (HERMES) between Nov. 3 2015 and Jan. 28, 2016. The observations were performed at the Roque de los Muchachos Observatory (La Palma, Islas Canarias, Spain) using the 1.2 m Mercator Telescope. HERMES is fed by optical fibres from the telescope. The instrument has a spectral resolution of  $R \approx 85\,000$ , and covers a spectral range from 377 to 900 nm (Raskin et al. 2011). It is isolated and temperature-controlled, yielding excellent wavelength stability. For these observations, the high-resolution mode of HERMES was used, and Th-Ar-Ne calibration exposures were made at the beginning, middle, and end of the night. The exposure time was calculated to reach a signal-to-noise ratio ( $S/N$ ) of 25 or higher in the  $V$  band. The reduction of the spectra was performed using the fifth version of the HERMES pipeline, which includes barycentric correction.

## 2.2 Photometry

The Kilodegree Extremely Little Telescope (KELT) survey provides time-series photometric data for a large fraction of the sky via two small-aperture (42 mm) wide-field ( $26^\circ \times 26^\circ$ ) telescopes, with a northern location at Winer Observatory in Arizona in the United States, and a southern location at the South African Astronomical Observatory near Sutherland, South Africa (Pepper et al. 2007,

2012). The pass-band is roughly equivalent to a broadband  $R$  filter, and the typical cadence is approximately 30 minutes.

Non-astrophysical trends are corrected and outliers are removed from KELT light curves with the Trend Filtering Algorithm (TFA; Kovács et al. 2005) as implemented in the VARTOOLS package (Hartman 2012). The TFA-processed version of the KELT light curve for HD 34736 used here contains 2808 observations over a time baseline of  $\sim 5$  years (from 2010 to 2015).

The field containing HD 34736 was observed by the Transiting Exoplanet Survey Satellite (*TESS*, Ricker et al. 2014) in sectors 05 and 32, correspondingly, in 2018 and 2020. The light curves obtained using the Science Processing Operations Center pipeline (SPOC, only for sector 05) and the MIT Quick-Look Pipeline (QLP, for both sectors) are available for downloading through the interface of The Mikulski Archive for Space Telescopes (MAST)<sup>1</sup>.

Follow-up observations aimed at the identification of the quasi-periodic signal in the *TESS* data (Sec. C) were taken in two standard filters  $R_C$  and  $I_C$  with the DK154 telescope at the La Silla Observatory over 14 nights from December 2022 to January 2023.

## 3 DATA ANALYSIS AND RESULTS

### 3.1 Photometric variability

Frequency analysis of high-quality photometric data collected by *TESS* Sector 05 (from 2018) confirmed not only the presence of the  $1^d_{2799}$  period, compatible with the  $1^d_{29}$  period of magnetic field variability (Romanyuk et al. 2017), but also another independent photometric variation with the much shorter period of  $0^d_{52}$  (Semenko 2020). The following *TESS* Sector 32 observations from 2020 fully supported this revelation.

The *TESS* frequency spectrum (Fig. 1, black curve) is dominated by two systems of frequencies. The first set (red line) corresponds to a rotationally modulated signal with eleven harmonics. The second set (green line) also carries the signal of rotational modulation with more than seven harmonics.

Both periodic signals were found in the five-year KELT photometry. The corresponding frequency spectrum is shown in Fig. 2 as a black curve. We use these data to disentangle photometric variability and determine the ephemeris of both components. It is known that phase light curves of mCP stars obtained in filters with different effective wavelengths generally differ (e.g. Krtićka et al. 2019). However, we do not consider this because the KELT and *TESS* pass bands nearly coincide. The following semi-phenomenological analysis aims to model as accurately as possible the observed photometric variations of HD 34736 in the KELT and *TESS* filters and to isolate the rotational variabilities of both components of the binary star.

#### 3.1.1 Phenomenological model of light curves of the HD 34736 binary

The observed, chaotic-looking light curves of HD 34736 can be satisfactorily interpreted as the sum of two strictly periodic light curves with the instantaneous periods  $P_A(t_A, \gamma_A)$  and  $P_B(t_B, \gamma_B)$ , and corresponding phase functions  $\vartheta(t_A, \gamma_A)$  and  $\vartheta(t_B, \gamma_B)$ , where  $t_A, t_B$  are times of observation corrected for Light Travel Time Delay (LTTD) of individual binary components  $A$  and  $B$ , as defined in Appendices A and B.

The thorough analysis of *TESS* and KELT data shows that the

<sup>1</sup> <https://dx.doi.org/10.17909/T9RP4V>

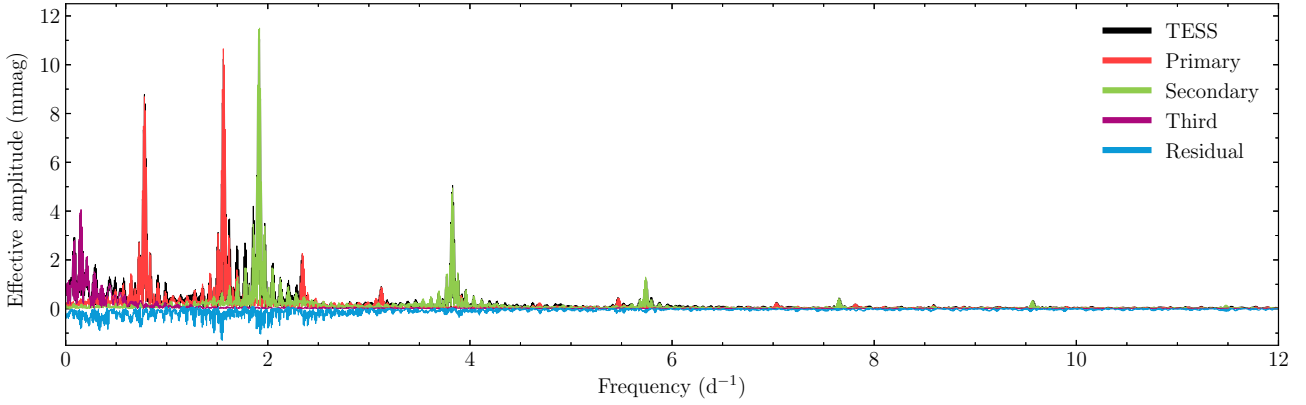


**Figure 1.** Complex amplitude periodogram of the HD 34736 *TESS* variability, in which a total of three sources participate: both components of the SB2 binary HD 34736 and a highly variable young star located close to the studied system. The light of the primary component of the binary shows a rotational modulation with a period of  $1^d280$  (orange line), and the light of the secondary changes with a rotational period of  $0^d523$  days (green line). The third component, identified with nearby variable UCAC4 414-008437, shows semi-regular changes (purple line) on a scale of several days (details are in Sec. C). A solid blue line shows the residuals.

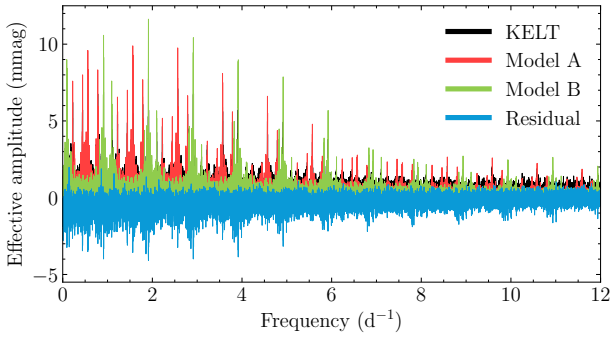


**Figure 2.** The amplitude periodogram of KELT data (black line) displays a dense forest of peaks; nevertheless, the positions of all of them can be explained by two basic frequencies  $f_A$ ,  $f_B$  and a lot of harmonics and aliases of the two-component model function (Eq. 3). The model predictions based on the analysis of *TESS* data are systematically higher. Residuals are shown by a solid blue line.

periods of both components undergo secular, more or less linear changes in time, so we have to use a more complex period model also containing non-zero time derivatives of their periods. The orthogonal ephemeris parameters for individual binary components then have three vector components, especially  $\gamma_A = [M_{1A}; P_{1A}; \dot{P}_A]$  and  $\gamma_B = [M_{1B}; P_{1B}; \dot{P}_B]$  (see Sec. A3). Then

$$\vartheta_{1A} = \frac{t_A - M_{1A}}{P_{1A}}; \quad \vartheta_A = \vartheta_{1A} - \frac{\dot{P}_A}{2} (\vartheta_{1A} - \eta_{2A})(\vartheta_{1A} - \eta_{3A}); \quad (1)$$

$$\vartheta_{1B} = \frac{t_B - M_{1B}}{P_{1B}}; \quad \vartheta_B = \vartheta_{1B} - \frac{\dot{P}_B}{2} (\vartheta_{1B} - \eta_{2B})(\vartheta_{1B} - \eta_{3B}), \quad (2)$$

where  $\eta_2, \eta_3$  are orthogonalization coefficients expressing data time distributions (Sec. A3 and Table 1).

The underlying light curves of both components are complex. They can be described by a harmonic polynomial of  $m_A = 11$  and  $m_B = 7$  orders, typical of mCP stars with complex surface photometric spot geometries and the presence of semi-transparent structures trapped in co-rotating stellar magnetospheres (Mikulášek et al. 2020; Krtićka et al. 2022). The light curve of an individual binary component of

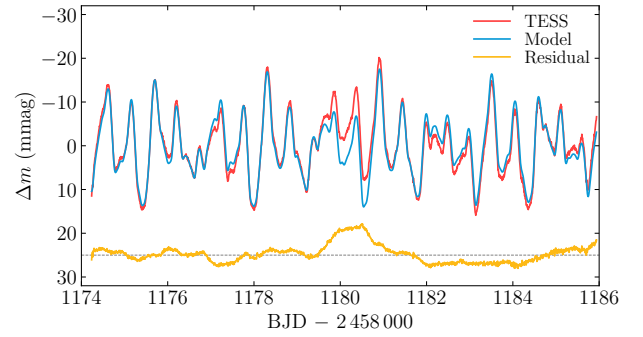


**Figure 3.** The first part of the *TESS* light curve of HD 34736 taken in Sector 32 (red line) modelled as the sum of two strictly periodic variations (blue line) and their residual (orange line) shifted by 25 mmag.

such type can be explicitly evaluated using special harmonic polynomials (SHP)  $\Xi(\vartheta, \mathbf{b})$  (See Sec. A4).

KELT and *TESS* photometry differ in how data are obtained and in the following basic reductions. However, as their effective wavelengths are nearly the same, we can assume the resulting light curve  $F(t, \alpha)$  of HD 34736 in the simple form:

$$F(t, \alpha) = \bar{m} + \Xi(\vartheta_A, \mathbf{b}_A) + \Xi(\vartheta_B, \mathbf{b}_B). \quad (3)$$

The vector of free parameters  $\alpha$  with 44 elements of the model of the observed light curve  $F(t, \alpha)$  including their uncertainties, can be determined using standard  $\chi^2$  minimization:

$$\chi^2 = \sum_{i=1}^n \frac{[y_i - F(t_i, \alpha)]^2}{\sigma_i^2}; \quad \frac{\partial \chi^2}{\partial \alpha} = \mathbf{0}, \quad (4)$$

where  $n$  is the total number of the photometric observation used,  $t_i$  is the HJD time of the  $i$ -th individual observation,  $y_i$  is its magnitude corrected for instrumental trends, and  $\sigma_i$  is the estimate of its internal uncertainty. The vector constraint that the quantity  $\chi^2$  is minimal gives 44 non-linear equations of 44 unknowns, which can be solved using standard iterative methods.

The analysis of residuals of the fit of the observed *TESS* light curve by the two-component model function  $F(t, \alpha)$  shows an unexpectedly

**Table 1.** The light curve ephemeris of *A* and *B* components. The meaning of parameters of the quadratic orthogonal fit are specified in Sec. A3.

$M_{1A} = 2\,458\,732.907\,0(5)$	$M_{1B} = 2\,458\,775.300\,0(5)$
$P_{1A} = 1^{\text{d}}279\,988\,5(11)$	$P_{1B} = 0^{\text{d}}522\,693\,8(5)$
$\dot{P}_A = 3.98(17) \times 10^{-8}$	$\dot{P}_B = -4.4(9) \times 10^{-9}$
$\eta_{2A} = -1191.2$	$\eta_{2B} = -2172.7$
$\eta_{3A} = 169.2$	$\eta_{3B} = 388.6$
$A_{\text{eff}A} = 14.1 \text{ mmag}$	$A_{\text{eff}B} = 13.0 \text{ mmag}$

high scatter of 2.7 mmag, while the true *TESS* photometry accuracy should be at least eight times better. We propose that the cause of this discrepancy is that the light of HD 34736 is contaminated by a nearby fainter, strongly variable star. The contribution to the variability of HD 34736 is considerable, and it causes additional semi-regular variations on the time scale of several days, sometimes reaching more than six mmag as shown in Fig. 3. The frequencies and amplitudes of the parasitic light variations can also be seen in the amplitude periodogram in Fig. 1 as a purple line. We have identified the source of invading variability as a young red pre-main-sequence star UCAC4 414-008437 (Appendix C).

### 3.1.2 Final light curve model solution. Disentangling of the light curve. Dips

We solve the set of equations given by (4) using *TESS* magnitudes corrected for the aperiodic variation of the third component to compute a final set of the model parameters. The result is shown in Fig. 4. Table 1 gives the final orthogonal ephemeris for both components. Using them, we can, for example, predict the moments of maximum brightness of individual components  $\Theta_A(E_A)$ ,  $\Theta_B(E_B)$  in the epochs  $E_A$ ,  $E_B$  from the point of view of an observer as follows:

$$\Theta_A = M_{1A} + P_{1A} E_A + \frac{P_{1A} \dot{P}_A}{2} (E_A - \eta_{2A})(E_A - \eta_{3A}) - \Delta t_A; \quad (5)$$

$$\Theta_B = M_{1B} + P_{1B} E_B + \frac{P_{1B} \dot{P}_B}{2} (E_B - \eta_{2B})(E_B - \eta_{3B}) - \Delta t_B, \quad (6)$$

where  $\Delta t_A$  and  $\Delta t_B$  are corrections for LTTD for individual components orbiting in a binary (Appendix B).

Using the final model of the light curve, we can disentangle the light curves of individual components and plot the phased light curves for both components (Fig. 5). The *A* phased light curves defined by the observation or bins of neighbouring observations in *TESS* and KELT colours are similar; only the amplitude of the latter is a bit smaller. The light curves are double-wave and rather complex, with at least five dips (Mikulášek et al. 2020) with amplitudes up to 1.5 mmag (Fig. 6). These details are probably caused by the presence of absorbing semitransparent structures confined in the co-rotating magnetosphere of the star (Krtićka et al. 2022). To empirically differentiate between surface inhomogeneities and circumstellar environment as two main drivers of the variability of CP stars with magnetospheres, we represent the observed light curves as the sum of fourth-degree harmonic polynomials emulating the contribution from spots and a finite number of relatively symmetrical dips appearing as Gaussian-like profiles and described by the phase of the centre, half-width, and depth. Standard regression analysis techniques can then be used to determine the light curve parameters. The dips depicted in Fig. 6 are obtained in this manner from the *TESS* photometry. The fourth-order polynomial fits are shown as the thin black lines in Fig. 5 for both components of HD 34736.

The effective amplitudes of the *A* and *B* components' contributions to the *TESS* light curve are  $A_{\text{eff}A} = 14.1 \text{ mmag}$  and  $A_{\text{eff}B} = 13.0 \text{ mmag}$  (Table 1). It is appropriate to remind at this point that for all phase light curves, especially in Fig. 5 and 6, we show only contributions to the total brightness of the system. The amplitude of the intrinsic variation of the sources is naturally different and depends on the luminosity.

### 3.1.3 Virtual O-C diagrams. Period changes

By finding non-zero time derivatives of the period of light changes for both system components, it is obvious that their rotation changes with time. To test the adequacy of the linear period change model used above, it is appropriate to visualize the observed period changes using the so-called virtual *O-C* diagrams, introduced and developed by Mikulášek et al. (2006, 2011a, 2012). In the mentioned method, it is assumed that the shape of the light curve is nearly constant, so changes in the instantaneous period will be manifested by a variable phase shift  $\Delta\varphi(t)$  of the observed light curve relative to the light curve that the star would have if its period remained constant. The instantaneous phase shift is then connected with the instantaneous *O-C*(*t*), as follows:  $O-C(t) = -P \Delta\varphi(t)$ , where *P* is a mean period.

To calculate the coordinates of the points plotted in the virtual *O-C*<sub>inA</sub> and *O-C*<sub>inB</sub> diagrams in Fig. 7 we divided the KELT and *TESS* data, sorted by observation time, into  $n_k = 8$  consecutive groups, characterized by the middle epoch  $E_{Ak}$  and  $E_{Bk}$  (see Table 2). We also introduced a new model of phase functions  $\vartheta_{kA}$ ,  $\vartheta_{kB}$  with fixed values of parameters  $M_{1A}$ ,  $M_{1B}$ ,  $P_{1A}$ ,  $P_{1B}$ , valid for a particular *k* and  $2n_k = 16$  free parameters: *O-C*<sub>kA</sub>, *O-C*<sub>kB</sub>:

$$\vartheta_{kA} = \frac{t_{kA} - M_{1A} - O-C_{kA}}{P_{1A}}; \quad \vartheta_{kB} = \frac{t_{kB} - M_{1B} - O-C_{kB}}{P_{1B}}; \quad (7)$$

$$k = 1, 2, \dots, n_k.$$

Parameters *O-C*<sub>kA</sub>, *O-C*<sub>kB</sub>, including their uncertainties, were calculated using a standard minimalization of the  $\chi^2$  (see Eq. 4). They are given in Table 2, together with virtual times of zero-th phase/light curve maximum moments  $O_{Ak}$  and  $O_{Bk}$  for epochs  $E_{Ak}$  and  $E_{Bk}$ , respectively, where:

$$O_{Ak} = O-C_{kA} + M_{1A} + P_{1A} E_{Ak};$$

$$O_{Bk} = O-C_{kB} + M_{1B} + P_{1B} E_{Bk}. \quad (8)$$

The virtual *O-C* diagrams show beyond any doubt that the angular velocities of both components of HD 34736 are changing, with the *A* component currently having the highest rate of change among all known mCP stars with variable rotation (Mikulasek et al. 2021). A linear increase in the rotation period derived here is highly credible. In the case of the *B* component, a monotonous acceleration of the rotation is noticeable, while a linear decrease in the rotation period appears to be a good initial hypothesis. The fact that the changes in periods are opposite essentially excludes any explanation involving the gravitational action of an invisible, distant third component.

## 3.2 Spectroscopic and spectropolarimetric analysis

As the échelle spectra of HD 34736 constitute a significant element of the available spectroscopic material, exploiting their wide spectral coverage using a multiline technique to increase the signal-to-noise ratio was natural. Before proceeding to the results, we describe the technique employed in the current study.

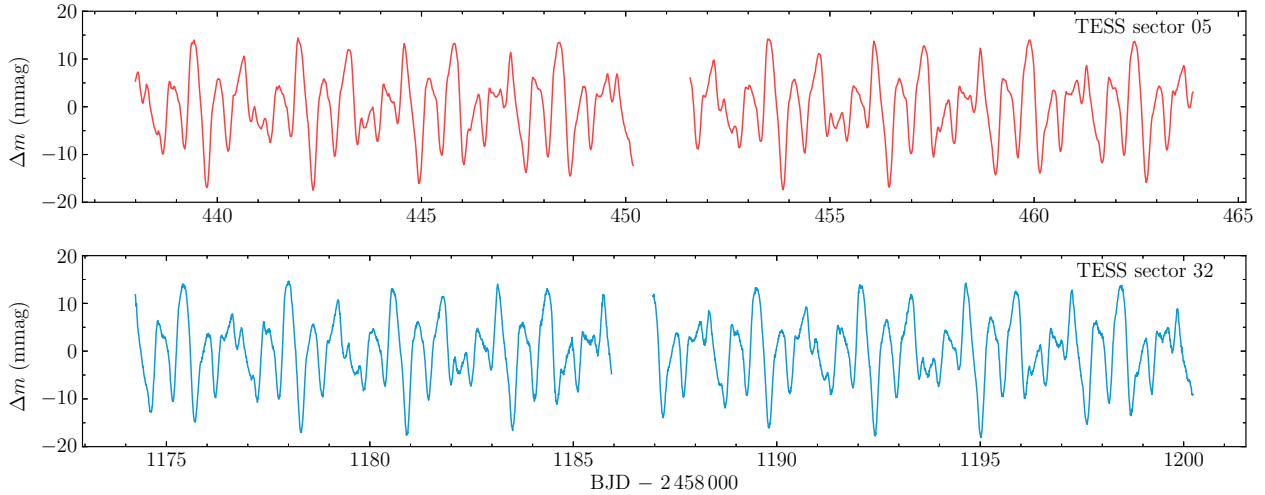


**Figure 4.** *TESS* light curves (Sector 05 — upper part, and Sector 32 — bottom part) corrected for aperiodic variation of the parasitic light of the third component.

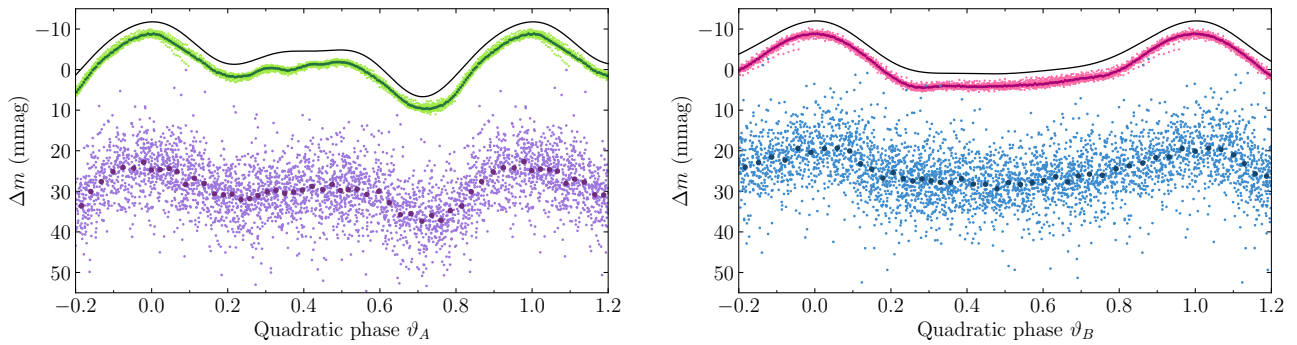


**Figure 5.** Corrected, disentangled, and phased *TESS* (upper curve) and *KELT* (lower curve) photometry of the *A* (left panel) and *B* components (right panel). Bins of about a hundred neighbourhood observations (dark dots) represent both components' mean light curves. The quadratic ephemerides of both components are given in Table 1. Black thin lines shifted by 3 mmag from corresponding *TESS* curves show the variants of fit made as the sum of a harmonic polynomial of the fourth degree, which was used for deriving dips.

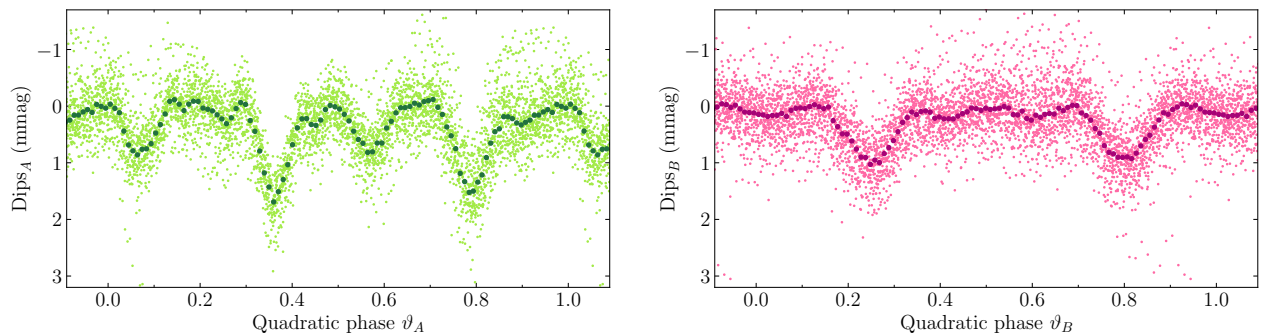


**Figure 6.** Dips in *TESS* light curves of *A* (left) and *B* (right) components in mmags. Darker points are bins of reduced photometric observations.

### 3.2.1 LSD profile analysis of échelle spectra

We have calculated the least-squares deconvolved (LSD) profiles for the échelle spectra of HD 34736 using the code described by Kochukhov et al. (2010). The line mask employed for these calculations was extracted from the Vienna Atomic Line Database (VALD,

Piskunov et al. 1995; Kupka et al. 1999; Ryabchikova et al. 2015; Pakhomov et al. 2019) for the parameters and composition of the magnetic primary presented by Paper I. The final mask includes 338 metal lines with a central depth exceeding 10% of the continuum in the 400–700 nm wavelength range. The mask is characterized by a

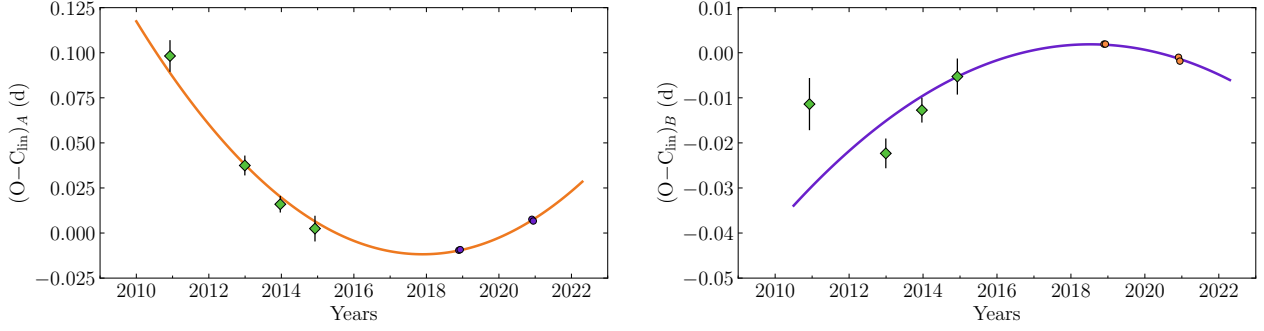


**Figure 7.** Dependence of phase shift between the observed light curves and the linear ephemeris prediction  $(O-C_{\text{lin}})_A$  (left) and  $(O-C_{\text{lin}})_B$  (right) in days versus time in years for A, B binary components. The fits of the dependence by parabola with  $\dot{P}_A = 3.98(17) \times 10^{-8} = 1.26(6) \text{ s yr}^{-1}$ ,  $\dot{P}_B = -4.4(9) \times 10^{-9} = -0.14(3) \text{ s yr}^{-1}$  are shown as solid curves. TESS observations are denoted as circles, while KELT ones are diamonds.

**Table 2.** Data from KELT and TESS 05, 32 photometries, for A and B components, corrected for the variability of the other components, were divided into eight consequent groups of  $N$  observations with the averages in ‘Years’ end mean epochs  $E_A$ ,  $E_B$  according to the ephemeris of the relevant components.  $(O-C_{\text{lin}})_A$  and  $(O-C_{\text{lin}})_B$  are mean differences between the observed moment of the particular component light maximum/instantaneous zero-th phase and its prediction according to the linear ephemeris models (see Fig. 7).  $O_A$ ,  $O_B$  are the times of the light maxima A and B components for the epoch  $E_A$  and  $E_B$ .

Year	Source	$N$	$E_A$	$(O-C_{\text{lin}})_A$	$O_A - 2450000$	$E_B$	$(O-C_{\text{lin}})_B$	$O_B - 2450000$
2011	KELT 1	457	-2499	0.098(9)	5 534.314	-6201	-0.011(6)	5 534.065
2013	KELT 2	857	-1910	0.038(6)	6 288.166	-4758	-0.022(4)	6 288.301
2014	KELT 3	955	-1631	0.016(5)	6 645.262	-4076	-0.013(3)	6 644.788
2015	KELT 4	539	-1358	0.002(7)	6 994.685	-3406	-0.005(5)	6 995.000
2019	TESS 05, I	582	-226	-0.0095(12)	8 443.6200	-634	0.0019(5)	8 443.9141
2019	TESS 05, II	595	-215	-0.0092(12)	8 457.7002	-608	0.0019(5)	8 457.5042
2021	TESS 32, I	1685	349	0.0076(12)	9 179.6306	774	-0.0010(5)	9 179.8640
2021	TESS 32, II	1912	360	0.0067(12)	9 193.7095	800	-0.0019(5)	9 193.4532

mean wavelength of 516.5 nm and a mean effective Landé factor of 1.16. In Fig. 8, we show the resulting Stokes  $I$  and  $V$  (for ESPaDOnS data) and Stokes  $I$  (for HERMES observations) LSD profiles deconvolved from high-resolution spectra. These profiles are arranged according to the rotational phase of the primary calculated following prescriptions given in Sec. 3.1. The spectra are shifted in velocity to the reference frame of the primary star using the orbital solution discussed in Sec. 3.2.4.

The narrow component of the Stokes  $I$  LSD profiles, which corresponds to the contribution of the primary star, shows a moderately coherent variation with rotational phase, compatible with signatures expected for an inhomogeneous surface distribution of chemical elements. The incoherent variation, also evident in the Stokes  $I$  panel of Fig. 8, is due to the orbital radial velocity shifts and intrinsic variability of the broad-lined secondary.

The circular polarisation signatures of the primary are detected for all ESPaDOnS observations. These Stokes  $V$  LSD profiles exhibit a smooth rotational phase variation, indicating a globally-organised magnetic field topology on the primary star. At the same time, no conclusive evidence of polarisation signatures of the secondary is seen in the Stokes  $V$  LSD profile data. Magnetic properties of the components are examined in Sec. 3.2.2.

### 3.2.2 Magnetic field of HD 34736

The longitudinal field  $\langle B_z \rangle$  of the narrow lined component was measured from the first moment of the Stokes  $V$  LSD profiles deconvolved

from ESPaDOnS spectra according to Wade et al. (2000) and Kochukhov et al. (2010), or using the techniques described by Semenko et al. (2022) and Monin et al. (2012) in the case of low-resolution spectropolarimetry from SAO and DAO, respectively. The three distinct methods yield typical uncertainties ranging from 100 to 800 G. Table 1 contains the full collection of measurements.

The observed longitudinal field varies with a period that is compatible with the photometrically-derived period  $P_{1A}$  (Table 1). Therefore, we interpret this variation as a consequence of the solid-body rotation of a star (chemically peculiar component A) with a magnetic field frozen in its outer atmospheric layers. Individual values of  $\langle B_z \rangle$  against the quadratic rotational phase are plotted in Fig. 9.

The phase curve of magnetic field variations is somewhat atypical, indicating a complex configuration of the global magnetic field with non-negligible high-order components and the effect of chemical abundance spots. The effective amplitude of changes in the  $\langle B_z \rangle$  component of the magnetic field is also unusually high: 9.3 kG.

Assuming a simple oblique dipolar field geometry (Stibbs 1950; Preston 1967), and by interpolating the isochrones for  $[\text{Fe}/\text{H}] = 0$  produced by the project MESA Isochrones & Stellar Tracks<sup>2</sup> (MIST, Dotter 2016; Choi et al. 2016), we have assessed the strength and obliquity of the magnetic field in the primary component of HD 34736. For this, we use  $R = 2.05 \pm 0.06 R_\odot$  as the appropriate theoretical value for a young star of the age of 4.6 Myr (average age of the subgroup Ori OB1c, Brown et al. 1994; Semenko

<sup>2</sup> <https://waps.cfa.harvard.edu/MIST/>

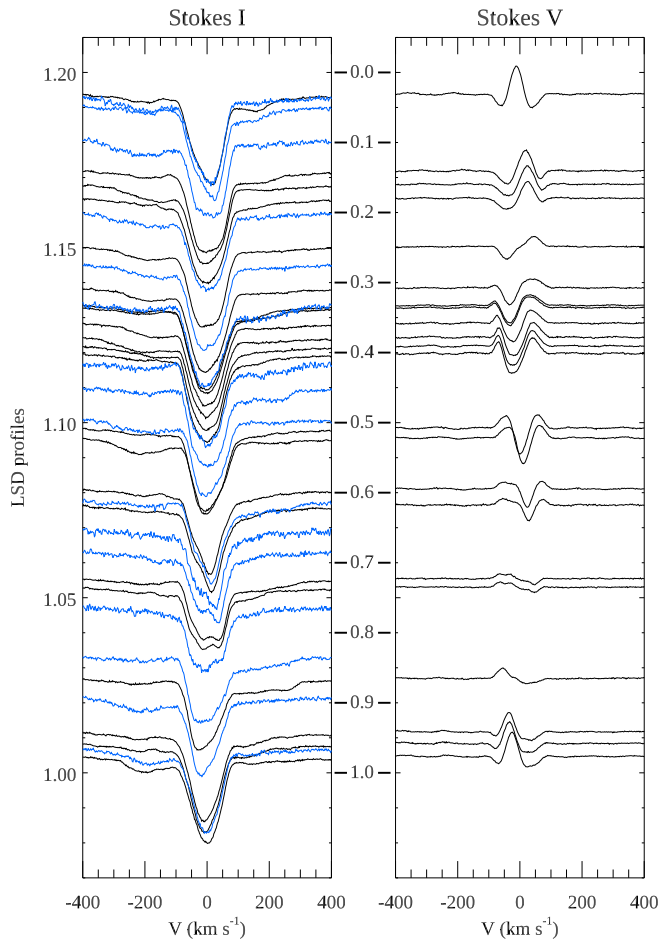


**Figure 8.** The composite LSD Stokes *I* (left panel) and Stokes *V* (right panel) profiles of HD 34736 derived from high-resolution spectra. The smooth black curves in the left panel correspond to the ESPaDO nS observations, while the blue curves show LSD profiles derived from the HERMES data. The spectra are shifted in velocity to the reference frame of the primary and are offset vertically according to its rotational phase (indicated between the panels).

et al. 2022) with an effective temperature of the magnetic primary ( $T_{\text{eff}} = 13\,000 \pm 500$  K, Sec. 3.2.3). Substituting this value for  $R$  and  $P_{\text{rot}} = P_{1A} = 1^{\text{d}}.2799885$  into the equation for equatorial rotational velocity

$$v_e = \frac{50.6 R [R_{\odot}]}{P_{\text{rot}} [\text{days}]}, \quad (9)$$

we find  $v_e = 81 \pm 3$  km s $^{-1}$ , which together with the spectroscopically measured  $v_e \sin i = 75 \pm 3$  km s $^{-1}$  (Sec. 3.2.3) gives us the inclination angle  $i = 68 \pm 7^{\circ}$ . Then, considering the extrema of the longitudinal magnetic field ( $\approx -6/+5$  kG), one can evaluate the polar strength  $B_d$  of the field as  $18.9 \pm 0.8$  kG and the angle  $\beta$  between the magnetic and rotational axes as  $83 \pm 2^{\circ}$ . The approach applied here is not ideal, but it allows us to derive approximate parameters of the stellar magnetic field in the simplest and fastest way.

A more accurate picture of the surface magnetic structure of the primary component of HD 34736 has been obtained using the Zeeman Doppler imaging (ZDI) magnetic tomography technique (Kochukhov 2016). This modelling is based on the mean metal line LSD profiles, illustrated in Fig. 8, derived from the 22 ESPaDO nS circular polarisation observations. Considering the complex composite nature of the spectral variability of HD 34736, with contributions

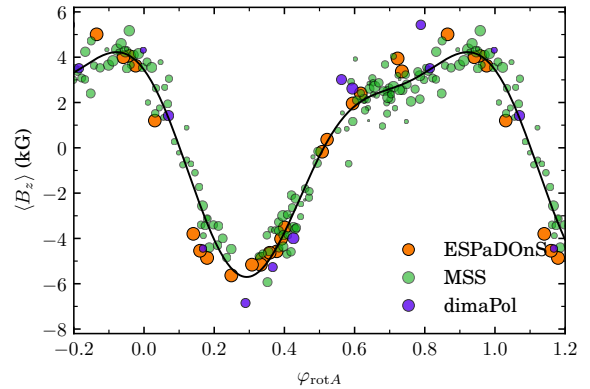


**Figure 9.** The observed  $\langle B_z \rangle$  variation versus quadratic rotational phase of the primary component. The areas of the symbols are proportional to the weight of  $\langle B_z \rangle$  measurements. The second-order harmonic polynomial fit is shown with the solid line.

from the variability due to spots on the primary, secondary, and the orbital motion of the two stars in an eccentric orbit, we chose not to pursue a detailed, simultaneous mapping of individual chemical elements and magnetic field (e.g. Kochukhov et al. 2014; Oksala et al. 2018). Instead, we model the mean Stokes *V* profiles of the narrow-lined primary, ignoring its surface spots and neglecting blending by the broad-lined secondary but correcting for the orbital radial velocity shifts. This approach is justified considering that variability of the majority of lines in the spectrum of the primary is relatively weak compared to high-amplitude changes seen in well-studied Ap stars with high-contrast chemical spots (e.g. Kochukhov et al. 2004; Silvester et al. 2012; Rusomarov et al. 2016). Furthermore, its mean Stokes *V* LSD profiles are smooth. They are characterised by a simple shape, lacking any small-scale features that are typical of polarisation spectra of fast-rotating magnetic stars with highly non-uniform surfaces (Kochukhov et al. 2017, 2019). All these factors indicate that chemical inhomogeneities do not significantly affect the shape and variability of the mean metal line Stokes *V* LSD profile of the primary.

Similar to ZDI studies of cool stars (Hackman et al. 2016; Rosén et al. 2016; Kochukhov & Shulyak 2019), we adopt the Unno-Rachkovsky solution of the polarised radiative transfer equation in the Milne-Eddington approximation to describe the local Stokes profiles. The line parameters required by this local line profile model were chosen to match the mean wavelength and Landé factor of the LSD line mask, whereas the local equivalent width was adjusted to fit the mean Stokes *I* spectrum. An inclination angle  $i = 60^{\circ}$  and projected rotational velocity  $v_e \sin i = 75$  km s $^{-1}$  were adopted for the magnetic mapping of the primary. No correction for continuum dilution is required since the decrease of the Stokes *V* amplitude is compensated by the decrease of the Stokes *I* line depth.

The magnetic field distribution obtained for HD 34736 with the ZDI code INVERS LSD (Kochukhov et al. 2014) is presented in Fig. 10. The primary possesses a strong, distorted dipolar global field geometry, characterised by a large asymmetry between the negative and positive magnetic hemispheres. The strong-field negative magnetic region exhibits a pair of magnetic spots with a local field strength reaching 19.6 kG. The overall mean field strength (averaged over the entire stellar surface) is 7.6 kG. The mean field modulus varies between 6.3 and 11.5 kG, depending on the rotational phase. The phase-averaged value of  $\langle B \rangle$  is 8.9 kG.



The ZDI code employed here uses a generalised spherical harmonic expansion to parameterise stellar surface field vector maps (see Kochukhov et al. 2014). This allows us to readily characterise contributions of different spherical harmonic modes to the global field topology of the primary. Regarding the magnetic field energy, the largest contribution comes from the  $\ell = 1$  (dipole) component, which contributes 63% of the magnetic energy. All quadrupole ( $\ell = 2$ ) and octupole ( $\ell = 3$ ) modes are responsible for 22 and 7% of the energy, respectively. The field of HD 34736 is predominantly poloidal, with 88% of the field energy concentrated in the poloidal harmonic modes.

The final fit achieved by the ZDI code to the observed Stokes  $V$  LSD profiles is illustrated in the upper panels of Fig. 11. The model reproduces the morphology of the observed polarisation profiles well. We also compared the mean longitudinal magnetic field predicted by the ZDI model geometry with  $\langle B_z \rangle$  measurements (Fig. 12). As expected, the ESPaDOnS ( $B_z$ ) are very well reproduced. The agreement with other longitudinal field determinations is also reasonably good, considering their scatter. Fig. 12 also shows the predicted  $\langle B \rangle$  phase curve.

No conclusive evidence of a magnetic field has been found in the secondary from available spectropolarimetric data. However, we have collected a handful of facts indirectly indicating with a very high probability that the cooler companion star is potentially magnetic.

At first, the individual light curves extracted from *TESS* photometry show clear periodicities with dips, which are common for chemically peculiar stars harbouring magnetic fields of complex structure. The nature of the dips remains unclear, but as the most plausible explanation, the presence of semitransparent structures confined in the co-rotating magnetosphere of the stars was proposed by Mikulášek et al. (2020) and developed by Krtićka et al. (2022). In Fig. 13, we combined the *TESS* light curves of both components and the dips extracted from them using the techniques described in Sec. 3.1.2. To emphasize the location of the dips in the original light curves, we marked them with shaded bands. The fact that the amplitude and, especially, stability of dips in the light curve of the secondary star (left panels of Fig. 13) are comparable to those observed in the hotter component (right panels) with a very strong field supports the hypothesis that a magnetosphere also exists around the cooler component.

The second argument in favour of the magnetic nature of the secondary star is its accelerating rotation. Theoretical modelling of evolution in massive stars predicts a significant impact of the magnetic field, even of the order of a few hundred gauss, on the rotational properties of stars during their evolution on the main sequence (e.g. Meynet et al. 2011; Keszthelyi et al. 2019), whereas for the intermediate-mass stars, such calculations have yet to be performed. Additionally, we cannot ignore evolutionary effects on the rotational rate as a  $2.7M_\odot$  star of the age of HD 34736 still evolves towards the ZAMS in the MIST models.

Eventually, we can examine the residuals of the primary magnetic curve for a possible correlation with the light curve of the secondary star. For this purpose, we have subtracted the smooth fit shown in Fig. 9 from the measured magnetic field. The residuals have been folded with the rotational period  $P_{1B}$  (Table 1) and smoothed using the running average. The result of this procedure is shown in the left bottom panel of Fig. 13. The position of two peaks, in this case, coincides well with the beginning and end of the flat section of the photometric curve. Although such coincidence cannot serve as a firm detection of the secondary's magnetic field, we consider it an indirect indicator that the fast-rotating component of HD 34736 may potentially have a longitudinal field  $\langle B_z \rangle$  order of 500 G. For comparison, the right bottom panel maps the dips' position on the

magnetic curve of the primary. Notably, for this component, the two most intense dips occur close to the extrema of the longitudinal field  $\langle B_z \rangle$ , while the phases of the remaining two dips cover the moments when the  $\langle B_z \rangle$  curve reverses sign.

In light of these results, we tentatively suggest that the secondary component of HD 34736 may be a rapidly rotating, weakly magnetic star similar to CU Vir (Mikulášek et al. 2011b; Kochukhov et al. 2014).

### 3.2.3 Physical parameters of the components

The atmospheric parameters of HD 34736 were first evaluated spectroscopically in Paper I. That research led to a two-star solution with the following parameters:  $T_{\text{eff}A} = 13\,700$  K,  $T_{\text{eff}B} = 11\,500$  K,  $\log g_A = \log g_B = 4.0$ , and  $v_e \sin i (A) = 73 \pm 7$  km s $^{-1}$ ,  $v_e \sin i (B) \geq 90$  km s $^{-1}$ . With the new observational material covering a broader range of wavelengths and rotational and orbital phases, we decided to revise our previous findings.

First, the projected rotational velocity  $v_e \sin i$  has been re-evaluated using two different techniques. The spectrum synthesis of two Fe II lines at 450.8 nm and 452.2 nm with low Landé factors made using the SYNTHMAG code (Kochukhov 2007) with the atmospheric parameters adopted from Paper I yields  $v_e \sin i = 75 \pm 3$  km s $^{-1}$ , in agreement with the previous estimate. Alternatively, fitting the mean Stokes  $I$  LSD profiles with the broadening function (Gray 2008), we obtain  $v_e \sin i$  larger by 2–3 km s $^{-1}$ . Neither of the two approaches can provide an unambiguous estimate for the secondary star. The resulting  $v_e \sin i$  of the broader-line component ranges from 110 to 180 km s $^{-1}$ . The wings of the Mg II 448.1 nm line in the composite spectrum at the orbital phase  $\varphi_{\text{orb}} = 0.1$  (Sec. 3.2.4) argue for the upper limit of the rotational velocity  $v_e \sin i \approx 180$  km s $^{-1}$  of the secondary star.

Next, we searched for a combination of  $T_{\text{eff}A}$ ,  $T_{\text{eff}B}$ , and  $R_A/R_B$  which would best fit the observed spectra in three regions containing hydrogen lines  $H_\alpha$ ,  $H_\beta$ , and  $H_\gamma$  at different orbital phases. The analysis was performed on the two ESPaDOnS spectra taken close to the moment of maximum amplitude of the radial velocity  $V_r$ . The optimal fit was achieved for  $T_{\text{eff}A} = 13\,000 \pm 500$  K,  $T_{\text{eff}B} = 11\,500 \pm 1\,000$  K, and  $R_A/R_B = 1.30 \pm 0.05$  (Fig. 14). As the hydrogen lines in the spectra of the early-type stars are equally sensitive to both  $T_{\text{eff}}$  and  $\log g$  and there are no reliable methods of independently constraining both parameters, we adopted  $\log g = 4.0$  as the lower limit at this stage of analysis. Considering the young age of HD 34736, the  $\log g$  value corresponding to the stellar mass and radius is very likely higher.

The spectroscopic parameters derived from hydrogen lines can be compared with the absolute magnitude computed from the *Gaia* Data Release 3 (DR3) parallax,  $\pi = 2.685 \pm 0.054$  mas (Gaia Collaboration et al. 2022). Assuming no interstellar extinction, the system's total magnitude is  $M_V = -0.02 \pm 0.05$ . This value can be reproduced with  $R_A = 2.17 \pm 0.08 R_\odot$  for the effective temperatures and the radii ratio inferred above. Adopting a moderate reddening of  $E(B-V) = 0.0248$  based on the Galactic model by Amôres & Lépine (2005) increases  $R_A$  by less than  $0.10 R_\odot$ . The resulting radius for the primary is reasonably consistent with evolutionary model predictions for young dwarfs with a  $T_{\text{eff}}$  of 13 000 as explained in Sec. 3.2.2. On the other hand, the surface gravity  $\log g = 4.0$  adopted for the hydrogen line fitting is too low for stars at this evolutionary stage. This discrepancy may be explained by the impact of an enhanced metallicity and deficient helium on the hydrogen line profiles, which leads to an underestimation of  $\log g$  by up to 0.25 dex when not accounted for (Leone & Manfre 1997).

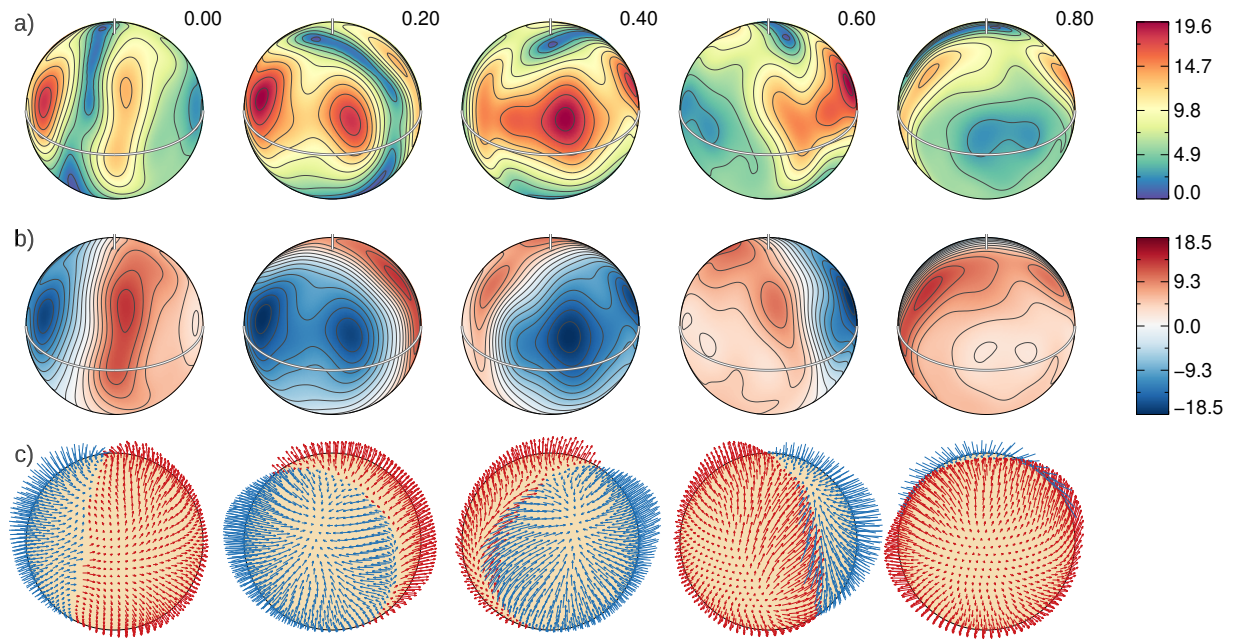


**Figure 10.** Magnetic field topology of the primary component of HD 34736 derived using with ZDI. The star is shown at five rotation phases, indicated above each spherical plot column. The spherical plot rows present the maps of a) field modulus, b) radial field, and c) field orientation. The contours over these maps are plotted with a 2 kG step. The vertical bar and thick line indicate the positions of the visible pole and rotational equator, respectively. The colour bars give the field strength in kG. The two colours in the field orientation map correspond to the field vectors directed outwards (red) and inwards (blue).

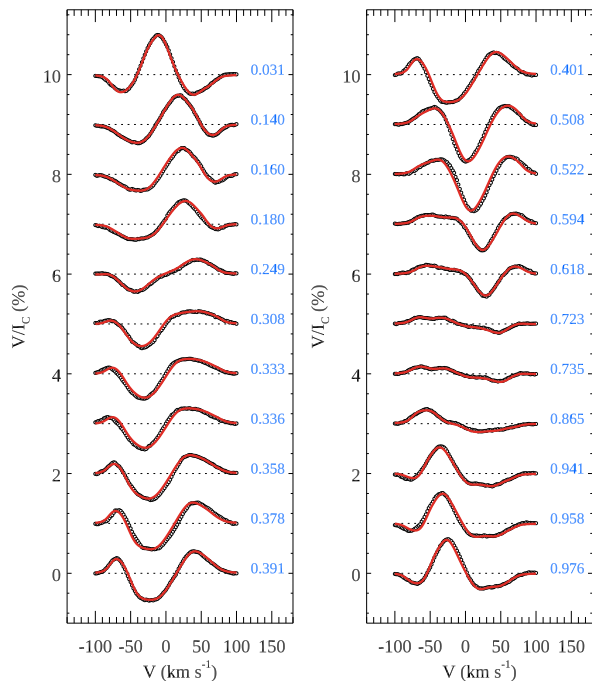


**Figure 11.** Comparison between the observed Stokes  $V$  LSD profiles (open symbols) and the ZDI fit (red solid lines). The spectra are offset vertically and arranged according to the primary's rotational phase, which is indicated to the right of each profile.

We additionally attempted to cross-check the stellar parameters of the system by fitting theoretical models to the observed spectral energy distribution (SED). To do this, we calculated a grid of model atmospheres using the LLMODELS stellar model atmosphere code (Shulyak et al. 2004) with average abundances given in Table 3.

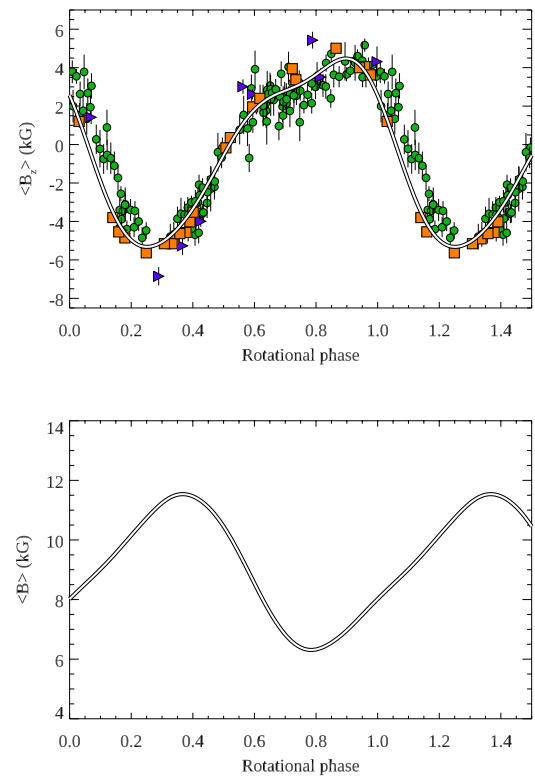


**Figure 12.** Upper panel: Comparison between  $\langle B_z \rangle$  measurements (symbols, colour scheme is to Fig. 9) and the longitudinal field variation predicted by the field distribution shown in Fig. 10. Lower panel: Predicted variation of the mean field modulus  $\langle B \rangle$ .

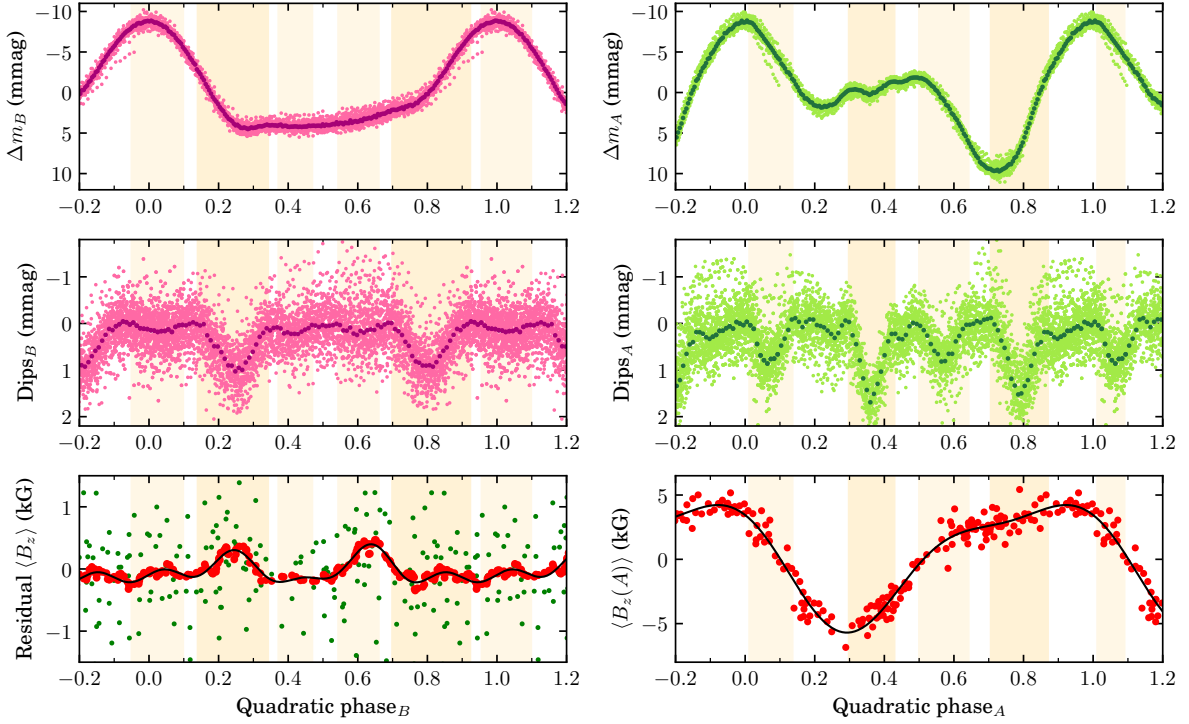


**Figure 13.** Top panels: *TESS* light curves of the components *B* (on the left) and *A* (on the right) obtained in this study. Middle panels: dips in the light curves of corresponding components. Bottom left panel: The raw (green dots) and smoothed using the running average (red circles) residual longitudinal magnetic field of HD 34736 as a phase of the rotational period  $P_B = 0.5226938$  days. Bottom right panel: the magnetic curve of the primary component. Thin black lines show the fits made using the low-order harmonic polynomials. Vertical shaded bands indicate the position of dips in the shown light and magnetic curves. More intensive dips are shown in darker colours.

We then optimized model parameters, such as the effective temperatures and stellar radii, to find a model that best fits the observed flux. Observations were taken from the *Gaia* DR3 ([Gaia Collaboration 2022](#)) where, for fitting purposes, we ignored fluxes below the Balmer jump due to calibration inaccuracies. Instead, we used observed broad-band UV fluxes obtained with the S2/68 telescope of the TD1 mission (European Space Research Organization (ESRO) satellite) ([Morgan et al. 1978](#)), complemented by data from the 2-Micron All-Sky Survey (2MASS, [Cutri et al. 2003](#)) for the infrared. Observations were transformed into absolute fluxes using the calibrations given by [Cohen et al. \(2003\)](#).

The predicted and observed energy distributions are compared in Fig. 15. In our SED fitting, we applied an interstellar extinction correction to  $E(B - V) = 0.0248$  and  $A_V = 0.0755$ , respectively.

First, assuming fixed parameters for the secondary,  $T_{\text{eff}B} = 11\,500$  K and  $R_B = 1.9 R_\odot$  (close to the value predicted by the ratio of spectroscopically derived radii) and ignoring the magnetic field, we find the best-fit model for the primary to have  $T_{\text{eff}A} = 12\,098 \pm 100$  K<sup>3</sup> and  $R_A = 2.23^{+0.15}_{-0.07} R_\odot$  which includes parallax uncertainty (red solid line in Fig. 15). We could not derive  $\log g$  from the available observations and thus kept it similar and fixed to  $\log g = 4.0$  for both components. While the derived radius of the primary agrees well with a previous spectroscopic estimate, the effective temperature that we

derive from fitting the SED is significantly lower (by about 900 K) than the spectroscopically derived value.

Including the magnetic field in the opacity and emerging flux calculation in our model atmospheres results only in a marginal increase of the effective temperature of the primary to  $T_{\text{eff}A} = 12\,152 \pm 100$  K (assuming surface average magnetic flux density  $\langle B \rangle = 7.6$  kG, Sec. 3.2.2), which is still too low compared to the spectroscopic estimate (see, for the details and implementation of the magnetic field in our stellar model atmospheres [Shulyak et al. 2008](#); [Khan & Shulyak 2006](#)).

We could achieve a better match between spectroscopy and SED for the primary but only assuming the secondary is cooler than 11 500 K. For instance, assuming  $T_{\text{eff}B} = 11\,000$  K,  $R_B = 1.9 R_\odot$  and calculating magnetic model atmospheres for the primary, we obtain  $T_{\text{eff}A} = 12\,400 \pm 100$  K,  $R_A = 2.24 \pm 0.02 R_\odot$  with a very similar fit quality as in the previous case of  $T_{\text{eff}B} = 11\,500$  K (red long-dashed line in Fig. 15).

Finally, assuming a single star model results in a good fit to the observed SED with stellar parameters  $T_{\text{eff}} = 11\,852 \pm 100$  K,  $R = 2.94 \pm 0.01 R_\odot$  (blue dashed line in Fig. 15).

The predicted flux calculated assuming spectroscopically derived parameters for the primary ( $T_{\text{eff}A} = 13\,000$  K) and secondary ( $T_{\text{eff}B} = 11\,500$  K) could not simultaneously match observations in all wavelength ranges (green dash-dot line in Fig. 15), where we again fixed the radius of the secondary to be  $R(B) = 1.9 R_\odot$ , while optimizing for the radius of the primary to match the observed points as closely as possible, which resulted in  $R_A = 1.93 R_\odot$ . We thus conclude that it is impossible to constrain robustly the parameters of both components solely from fitting the SED and a self-consistent

<sup>3</sup> This uncertainty is based solely on the errors of the *Gaia* spectrophotometry and does not include the errors for  $E(B - V)$ . After including the extinction model published by [Amôres & Lépine \(2005\)](#), the combined error of  $T_{\text{eff}A}$  increases to 365 K.

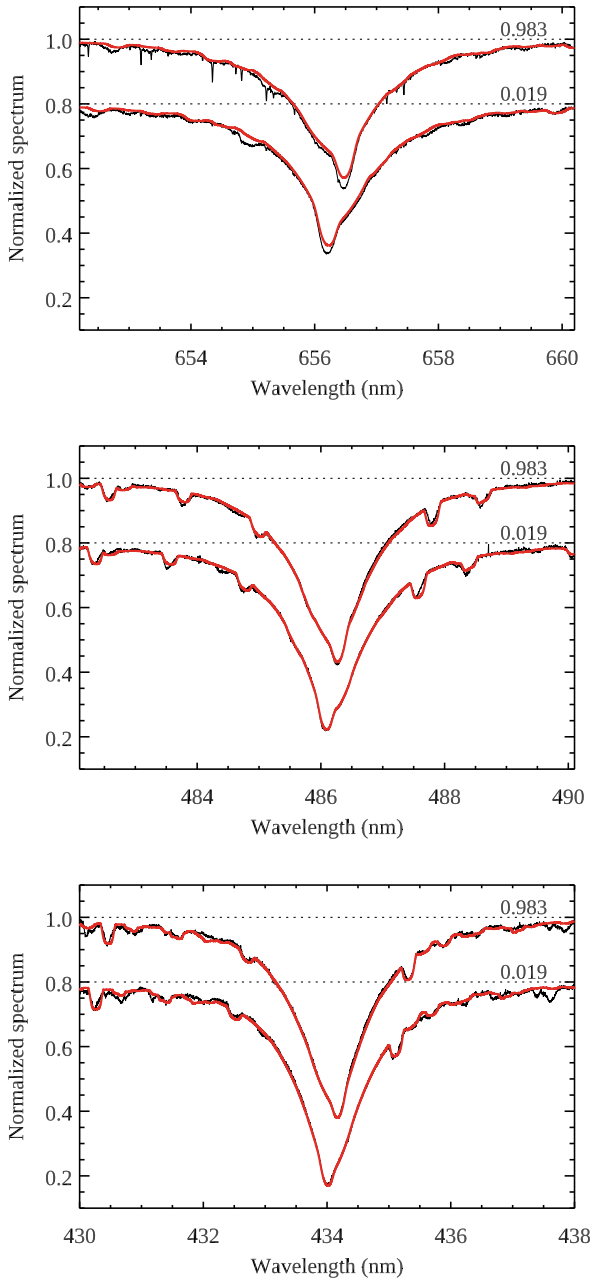


**Figure 14.** Observed hydrogen Balmer lines (thin black lines) compared with theoretical fit (thick red lines). The observed and model spectra are illustrated for two orbital phases close to periastron, with the second set offset vertically for display purpose.

approach similar to that used by, e.g., [Romanovskaya et al. \(2019, 2021\)](#) and [Shulyak et al. \(2013\)](#) would be needed, which, however, is out of the scope of the present paper.

[Roman \(1978\)](#) and [Renson & Manfroid \(2009\)](#) classified HD 34736 as a Si-type CP star. The presence of intense lines of singly ionised silicon (e.g. 412.9–413.0, 504.1, and 634.7–7.1 nm) in the spectrum of the magnetic component ostensibly supports this classification. However, careful inspection of stellar spectra also reveals variable and strengthened lines of chromium, titanium, and some rare-earth elements, which, together with weak helium lines, implies that the spectrum is more accurately classified as He-wk.

To quantify the peculiarities of the magnetic primary, we anal-

**Table 3.** Chemical composition of the primary component of HD 34736 evaluated with respect to the Sun ([Asplund et al. 2021](#)) at the rotational phases 0.773 and 0.272. Only one value is given when the corresponding abundance remains constant. The em-dashes indicate absent data.

Element	$\Delta\varepsilon$ , dex	
	$\varphi_{\text{rotA}} = 0.272$	$\varphi_{\text{rotA}} = 0.773$
He		-1.7
Mg	+0.2	-1.1
Al	0	—
Si		+0.9
Ti		+0.66
Cr	+1.4	+1.3
Fe	+0.7	+0.1
Pr	+3.9	—
Nd		+2.8
Dy	—	+3

ysed its chemical composition at two rotational phases when the magnetic field (Sec. 3.2.2, Fig. 9) was close to the minimum (HJD 2457331.665,  $\varphi_{\text{rotA}} = 0.272$ , HERMES) and maximum (HJD 2456967.515,  $\varphi_{\text{rotA}} = 0.773$ , MSS).

Spectra of both components were modelled with the SYNTHMAG code ([Kochukhov 2007](#)) in the LTE approximation and using up-to-date atomic data from the VALD database. A homogeneous magnetic field with a radial component  $B_r = 17$  kG was accounted for only in the main component. The microturbulent velocity was set to zero. ATLAS9 atmospheric models for both components were taken from the NEMO database ([Heiter et al. 2002](#)).

The spectrum of the magnetic component evolves with rotation. The largest variations are found for magnesium, chromium, and silicon. For example, between rotational phases  $\varphi_{\text{rotA}} \approx 0.272$  (corresponding approximately  $\langle B_z \rangle$  minimum) and  $\approx 0.773$  (corresponding to the plateau in the  $\langle B_z \rangle$  curve, Fig. 9), the abundance of magnesium varies by 1.1 dex. Iron demonstrates the opposite trend: at  $\varphi_{\text{rotA}} = 0.773$  its concentration is nearly solar ([Asplund et al. 2021](#)) and increases by 0.5 dex at  $\varphi_{\text{rotA}} = 0.272$ . The chromium abundance at both phases is approximately the same, but the profiles of the individual Cr lines are variable. We find silicon overabundant by 0.9 dex. Intensity of Si II lines at 623.2, 634.7, and 637.1 nm can be described assuming  $B_d \approx 24$  kG when  $\langle B_z \rangle$  is near minimum. The abundances derived from Si II lines differ from those from Si III lines in a way that is common for magnetic CP stars ([Bailey & Landstreet 2013](#)). The chemical composition of the narrow-lined magnetic component is summarized in Table 3. We estimate a typical error of about 0.1 dex for the abundances of most elements except praseodymium, which is as high as 0.5 dex. The main sources of error are the spectroscopic variability of both components and uncertainties in atmospheric parameters.

The broad-lined star is poorly represented in the composite spectra due to its fast rotation, making it impossible to assess its chemical peculiarities. We can only say that with  $v_e \sin i = 180$  km s<sup>-1</sup> adopted for the broad-lined component, this star should have magnesium overabundant by at least 0.5 dex relative to the solar value. The signatures of the intrinsic spectral variability of the companion star are visible only in the Mg II 448.1 nm and selected Si II lines at the orbital phases of the maximum Doppler separation.

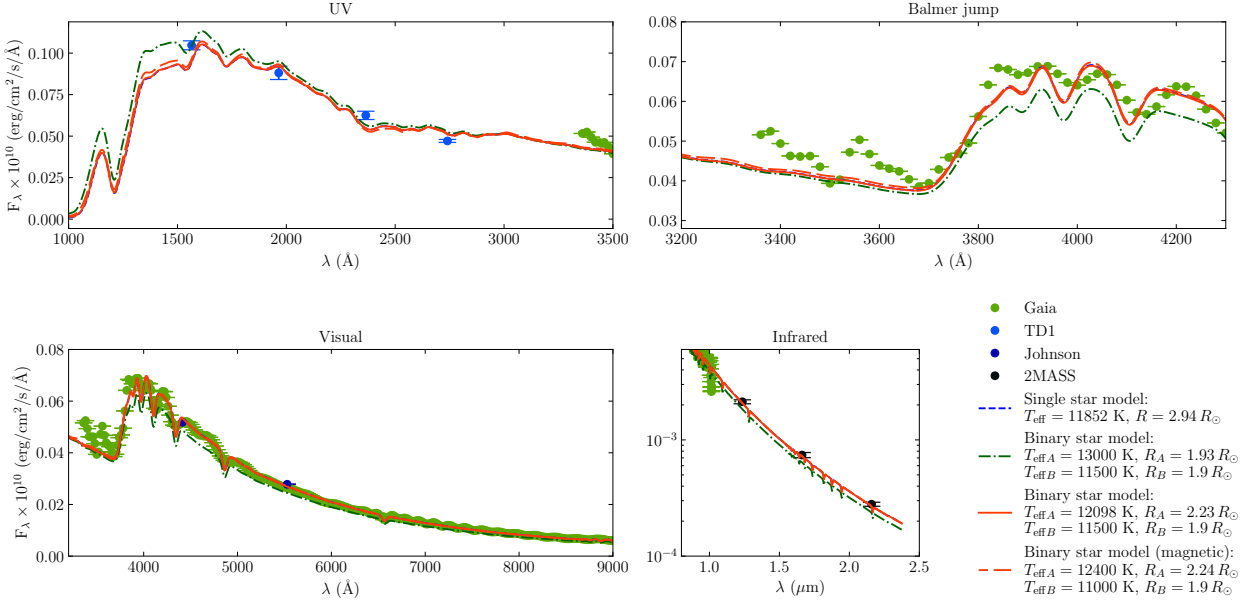


**Figure 15.** Comparison between observed and predicted flux at different wavelength domains. Note the logarithmic y-axis scale for the infrared flux (bottom right panel). See the plot legend for more details.

### 3.2.4 Stellar multiplicity

Paper I depicted HD 34736 as a double-lined spectroscopic binary (SB2) with an orbital period shorter than one day, which was tentatively proposed for the system based on the limited observations. In the current study, we comprehensively describe this SB2 system, including its orbital solution and possible multiplicity of higher order.

To measure the radial velocity  $V_r$  of the individual components, we primarily fit the mean LSD Stokes  $I$  profiles with a function defining the rotationally broadened profile (Gray 2008). For the few instances where two sets of lines were visible, the fitting function was a sum of two profiles. We preferred using a broadening function, as rotation dominates over the other line broadening mechanisms in the spectra of HD 34736. By averaging many lines from different elements, LSD, to some extent, alleviates the impact of a spotted surface on the derived  $V_r$ . Also, by using the broadening function for fitting, we give additional weight to the outer parts of the line to minimise the effects of spots, which mostly affect line cores.

At the same time, we approximate the Mg II 448.1 nm lines of both components with model spectra synthesised for the components' stellar parameters. Despite the inhomogeneous distribution of magnesium in HD 34736,  $V_r$  measured from this element shows better accuracy than hydrogen due to the profound blending of the components' hydrogen lines.

Individually measured radial velocities are listed in Table 1. For the primary component, we give only  $V_r$  measured from the LSD profiles  $V_r(A)_{\text{LSD}}$ . For the secondary star, where the magnesium line modelling works better in a broader range of orbital phases, we show both types of velocities denoted as  $V_r(B)_{\text{LSD}}$  and  $V_r(B)_{\text{MgII}}$ . As a conservative upper limit of error, in the case of  $V_r(B)_{\text{MgII}}$ , we adopted  $20 \text{ km s}^{-1}$ . This value includes uncertainties defined by the quality of input data (e.g., SNR and continuum normalisation) and accuracy of the atmospheric parameters. The radial velocities measured on the same night were averaged.

The final fit of velocities shown in Fig. 16 has been made using the programme RVFIT (Iglesias-Marzoa et al. 2015). In Table 4, we

**Table 4.** Orbital parameters HD 34736 derived from the observed radial velocity variation. The 2<sup>nd</sup> and 3<sup>rd</sup> columns show the results of fitting based on velocities measured using the Mg II 448.1 nm line and the LSD profiles, respectively.  $T_p$  is the moment of periastron.

Parameter	Value (Mg II)	Value (LSD)
$T_p$	2457415.3460 (0.003)	2457415.3481 (0.003)
$K_A$ ( $\text{km s}^{-1}$ )	69.74 (0.07)	69.74 (0.07)
$K_B$ ( $\text{km s}^{-1}$ )	99.57 (3.15)	111.63 (1.12)
$\gamma$ ( $\text{km s}^{-1}$ )	23.28 (0.05)	23.32 (0.05)
$P$ (days)	83.2193 (0.0030)	83.2183 (0.0035)
$e$	0.8103 (0.0003)	0.8104 (0.0003)
$\omega$ ( $^\circ$ )	84.2 (0.1)	84.3 (0.1)
$\text{RMS}_A$ ( $\text{km s}^{-1}$ )	4.86	4.87
$\text{RMS}_B$ ( $\text{km s}^{-1}$ )	17.92	19.76
$M_B/M_A$	0.70 (0.02)	0.62 (0.01)
$M_A \sin^3 i$ ( $M_\odot$ )	4.9 (0.3)	6.4 (0.1)
$M_B \sin^3 i$ ( $M_\odot$ )	3.5 (0.1)	4.0 (0.1)
$a_A \sin i$ ( $R_\odot$ )	67.2 (0.1)	67.2 (0.1)
$a_B \sin i$ ( $R_\odot$ )	95.9 (3.0)	107.5 (1.0)

provide two orbital solutions based on the radial velocities from Table 1 with each solution based on the different sources of radial velocities of the secondary component.

According to the best-fit solution, HD 34736 consists of two hot stars orbiting each other on highly eccentric orbits ( $e > 0.8$ ) with a period of 83 days. Interestingly, the rotation of the narrow-lined magnetic primary component is quasi-synchronised with its orbital motion; the ratio  $P_{\text{orb}}/P_{1A}$  is almost equal to 65. The primary has the projected mass  $M_A \sin^3 i = 4.9\text{--}6.4 M_\odot$ , where  $i$  is the inclination angle of the orbit. The mass  $M_B \sin^3 i$  of the companion is  $3.5\text{--}4.0 M_\odot$ . Such values typically characterise early and mid-B main sequence stars and appear systematically larger than those implied

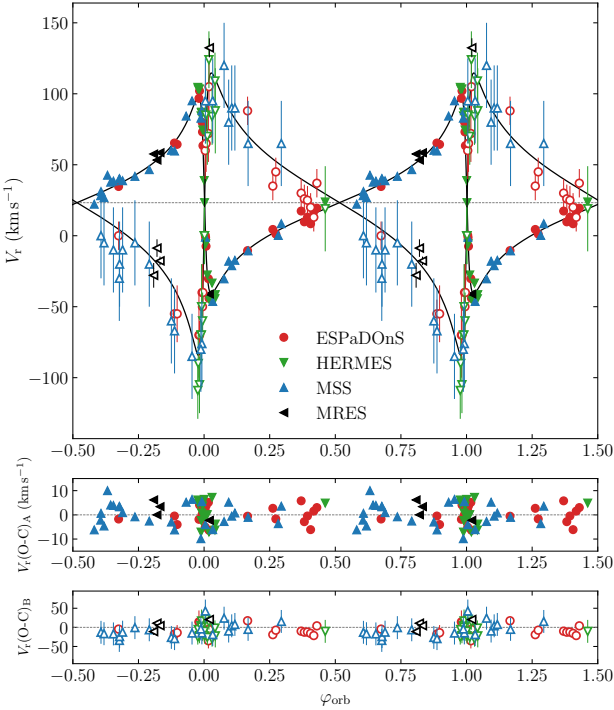


**Figure 16.** Measured radial velocities of the HD 34736 components plotted against the orbital phase computed for parameters from Table 4. Filled symbols correspond to the magnetic primary, and open symbols mark  $V_r$  of the secondary.

by the components' effective temperatures determined in Sec. 3.2.3. We address this problem in Sec. 4.

#### Is HD 34736 an eclipsing binary?

If the angle  $i$  were close to 90 degrees, the binary could undergo eclipses. Here, we will try to predict when these eclipses might occur during the orbit and estimate their parameters. To avoid misunderstandings, we will consistently distinguish between so-called *transits* when a smaller component  $B$  passes over the disc of component  $A$ , and *occultations* when a more prominent component  $A$  covers component  $B$  and can cover it entirely.

For the description of the motion of stars in a binary with parameters of orbital period  $P_{\text{orb}} = 83^d 219(3)$ , argument of periastron  $\omega = 1.4696(18)$  rad, eccentricity  $e = 0.8103(3)$ , and the basic moment of the periastron passage  $T_p$ , from the viewpoint of a distant observer, it is useful to introduce the orbital phase function  $\vartheta$ , the rectified phase function  $\vartheta_r$ , and their corresponding phases:  $\varphi$ , and

$\varphi_r$ , as follows:

$$M(t) = 2\pi \frac{t - T_p}{P_{\text{orb}}}; \quad (10)$$

$$\vartheta(t) = \frac{1}{2\pi} \left[ M(t) + \omega + \frac{\pi}{2} \right] = \frac{t - M_{\text{orb}}}{P_{\text{orb}}}; \quad (11)$$

$$M_{\text{orb}} = T_p - P_{\text{orb}} \left( \frac{\omega}{2\pi} + \frac{1}{4} \right) = 2457375.077(23);$$

$$\vartheta_r(t) = \frac{1}{2\pi} \left[ \vartheta(t) + \omega + \frac{\pi}{2} \right]; \quad \theta = 2\pi \vartheta_r - \omega - \frac{\pi}{2}; \quad (12)$$

$$\varphi = \vartheta - \text{floor}(\vartheta); \quad \varphi_r = \vartheta_r - \text{floor}(\vartheta_r); \quad (13)$$

$$r = \frac{a(1-e^2)}{1+e \cos \theta} = \frac{a(1-e^2)}{1+e \sin(2\pi \vartheta_r - \omega)}, \quad (14)$$

$$V_{rA,B}(t) = \gamma \pm K_{A,B} [\cos(\theta + \omega) + e \cos \omega] = \gamma \pm K_{A,B} [\sin(2\pi \vartheta_r) + e \cos \omega], \quad (15)$$

$M(t)$  is the mean anomaly in radians,  $\theta$  is the true anomaly, as defined by Eq. B2,  $r$  is the instantaneous separation of the components,  $a$  is the length of the semimajor axis,  $a = (A_A + A_B)/\sin i = 163(3)/\sin i R_{\odot}$ . The ratio between maximum and minimum separation of components is substantial –  $r_{\text{max}}/r_{\text{min}} = (1+e)/(1-e) = 9.543(17)$ . The distance of components is minimal when the stars pass periastron; this occurs if the both orbital and rectified phases equal  $\varphi_{\text{per}} = \varphi_{\text{rper}} = \frac{1}{2\pi} \omega + \frac{1}{4} = 0.4840(3)$  (see Eqs. (11), (12), and (13)). The orbital and rectified phases of the apastron passage are  $\varphi_{\text{ap}} = \varphi_{\text{rap}} = \frac{1}{2\pi} \omega + \frac{3}{4} = 0.9840(3)$ .

The moment of minimum brightness during the occultation corresponds to the moment of the *superior conjunction* of the binary star components, i.e., if the rectified phase  $\vartheta_r = 0$ . In contrast, the minimum brightness during the transit occurs when the binary components are in the *inferior conjunction*, and the rectified phase  $\vartheta_r$  equals 0.5. Hence the conditions for true anomalies  $\theta_{s,i}$  for superior/inferior conjunctions are:

$$\theta_{s,i} = 2\pi k - \omega \mp \frac{\pi}{2}, \quad (16)$$

where  $k$  is an integer. In the case of  $k = 0$ ,  $\theta_s = -3.0404(18)$  rad and  $\theta_i = 0.1012(18)$  rad. Combining Eqs. (B3) and (16), we obtain the corresponding values of eccentric anomalies of superior/inferior conjunctions  $E_{s,i}(\theta_{s,i})$  consecutively preceding/following the basic passage through periastron.

$$E_{s,i} = 2 \arctan \left[ \sqrt{\frac{1-e}{1+e}} \tan \left( \frac{\theta_{s,i}}{2} \right) \right]; \quad (17)$$

$$T_{s,i} = T_p + \frac{P_{\text{orb}}}{2\pi} (E_{s,i} - e \sin E_{s,i}), \quad (18)$$

$$\varphi_{s,i} = \frac{T_{s,i} - M_{\text{orb}}}{P_{\text{orb}}} - \text{floor} \left( \frac{T_{s,i} - M_{\text{orb}}}{P_{\text{orb}}} \right); \quad r_{s,i} = \frac{a(1-e^2)}{1 \mp e \sin \omega}; \quad (19)$$

Eccentric anomalies in superior/inferior conjunctions are  $E_s = -2.831(6)$  rad,  $E_i = 0.0328(6)$  rad, times of conjunction close to the basic periastron passage in BJD:  $T_s = 2457381.13(13)$ ,  $T_i = 2457415.428(3)$ , and corresponding phases  $\varphi$  according to (11) and (13) for center of occultations and transits are  $\varphi_s = 0.0727(16)$ , and  $\varphi_i = 0.4849$ .

In the case  $i = \pi/2$ ,  $a = A_A \sin^3 i + A_B \sin^3 i = 67.2(0.1) + 96(3) = 163(3) R_{\odot}$  and according to (19) the distance of components in occultation is  $r_s = 289 R_{\odot}$ , while during the transit it is only  $r_i = 31.0 R_{\odot}$ . To predict the eclipse widths and depths, we used the estimates of stellar parameters:  $R_A = 2.1 R_{\odot}$ ,  $R_B = 1.9 R_{\odot}$ ,

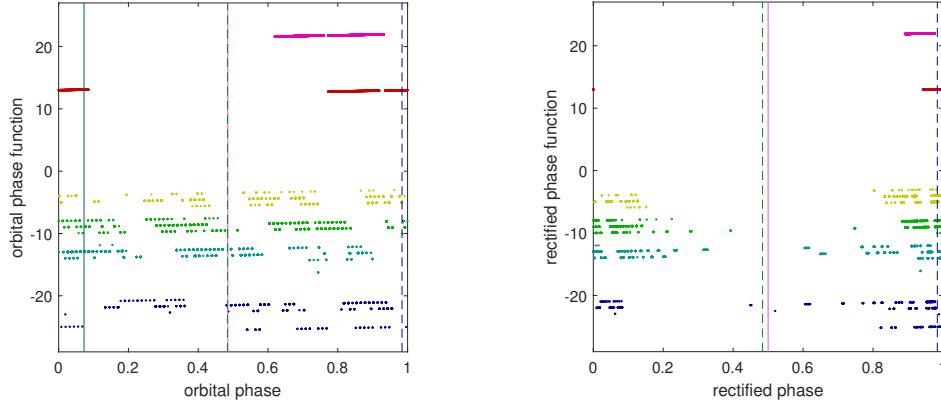


**Figure 17.** The distribution of moments of photometric observations with respect to the orbital motion of the components of the spectroscopic binary star HD 34736. The dependencies of (a) the orbital phase function  $\vartheta$  on the orbital phase  $\varphi$  and (b) the rectified phase function  $\vartheta_r$  on the rectified phase  $\varphi_r$ , as these quantities are defined in the equations 11, 12, and 13 are used for illustration. Observations *KELT* 1, 2, 3, and 4 (Table 2) are distinguished by the colour of markers from blue to yellow. *TESS* sector 05 and 32 observations are marked in red and magenta. Orbital phases are marked vertically when superior (green) and inferior (pink) conjunction occurs, and the passages of periastron and apastron are indicated in dashed lines. Possible occultations and transits occur at rectified phases 0 and 0.5. From Fig. (b), it is obvious that the observation does not cover the possible transit. On the other hand, the observation from *TESS* Sector 05 well covers the occultation.

$T_{\text{eff}}(\text{A}) = 13\,000\text{ K}$ ,  $T_{\text{eff}}(\text{B}) = 11\,500\text{ K}$ , from Sec. 3.2.3. The half-width of the occultation is 1.0 d (!), and its bolometric magnitude depth is 0.44 mag. This part of the light curve was well monitored by *TESS* observations in Sector 05; indeed, this occultation would not escape our notice. The transit minimum is even deeper — 0.86 mag, but it would happen literally in a flash — its half-width would be only 2.7 h. Our observations do not sufficiently cover this region of the light curve.

However, we emphasize that the visibility of occultations depends very dramatically on the actual inclination of the orbital plane. An occultation will only occur when  $i > 88.4^\circ$ . In the case of a transit, the situation is more favourable; to observe it, the inclination angle must be greater than  $76.5^\circ$ . However, there is a high probability that we will miss the transit given its brevity.

### 3.3 Radio and X-ray emission of HD 34736

#### 3.3.1 Radio observations

A radio source in the vicinity of HD 34736 was detected for the first time in the NRAO VLA Sky Survey (NVSS) and reported by Condon et al. (1998). An integrated flux density of the object NVSS J051920–072048 (field C0520M08) with coordinates  $\alpha_{J2000} = 05^{\text{h}}19^{\text{m}}20.98^{\text{s}}$ ,  $\delta_{J2000} = -07^\circ20'48.9''$  was measured as  $2.3 \pm 0.4\text{ mJy}$  at 1.4 GHz.

In the Very Large Array Sky Survey (VLASS, Lacy et al. 2020) archive, we found three observations (epochs 1.1, 2.1, and 3.1) of the sky area encompassing HD 34736 obtained at  $\nu \sim 3\text{ GHz}$  between 2017 and 2023. Appropriate quick-look images were downloaded from the archive of The Canadian Initiative for Radio Astronomy Data Analysis (CIRADA<sup>4</sup>) for measurement. The flux densities shown in Tab. 5 were obtained by fitting a two-dimensional Gaussian to the point source using the Common Astronomy Software Applications (CASA, McMullin et al. 2007). The error bars include the fitting error, the map rms and 10% of the flux density (attributed to uncertainty in the absolute flux density scale) added in quadrature.

<sup>4</sup> CIRADA Image Cutout Web Service. <http://cutouts.cirada.ca/>

**Table 5.** The flux densities  $S_\nu$  of the radio sources associated with HD 34736 in NVSS and VLASS observational data. The heliocentric Julian dates are calculated as an average of the first and the last scans’ times, as specified in the corresponding archives.  $\vartheta_{\text{A}}$  and  $\vartheta_{\text{B}}$  are quadratic rotational phases for components A and B, respectively.  $\varphi_{\text{orb}}$  is the orbital phase of the spectroscopic binary system.

Survey	HJD	$\vartheta_{\text{A}}$	$\vartheta_{\text{B}}$	$\varphi_{\text{orb}}$	$S_\nu$ (mJy)
NVSS	2449304.9288	0.403	0.247	0.542	$2.3 \pm 0.4$
VLASS1.1	2458085.8949	0.527	0.049	0.058	$2.2 \pm 0.3$
VLASS2.1	2459106.1033	0.561	0.876	0.317	$0.9 \pm 0.2$
VLASS3.1	2459974.7217	0.144	0.705	0.755	$1.0 \pm 0.2$

In the table, we included one earlier measurement of the radio flux of HD 34736 published by Condon et al. (1998).

The integrated flux of the radio source VLA J051921.23–072049.6 found at the position of the studied star in the VLASS data varies between different observations but remains significant at least within  $4\sigma$  (Fig. 18). The unprecedented pointing accuracy of the VLA leaves no doubt that the detected source is associated with HD 34736. After scaling to the distance to the star, the maximum radio luminosity  $L_{\text{R}}$  of the source is equal to  $4.3 \times 10^{17}\text{ erg s}^{-1}\text{ Hz}^{-1}$ .

#### 3.3.2 X-ray emission

It was Grillo et al. (1992) who first reported the detection of HD 34736 in X-rays. The authors observed B-type stars with the Imaging Proportional Counter (IPC) of the *Einstein* Observatory in the range of energies 0.16–4 keV, and concluded that X-ray emission with a luminosity  $L_{\text{X}} \geq 10^{30}\text{ erg s}^{-1}$  was common for B0–B3 stars, and became rare or non-existent towards B8–B9. For the studied star, a  $\log L_{\text{X}}$  expressed in  $\text{erg s}^{-1}$  was estimated as 30.59.

In August 1990, the region of the sky with HD 34736 was observed with the Position Sensitive Proportional Counters (PSPC) of the *ROSAT* spacecraft in the 0.1–2.4 keV range, seemingly with zero

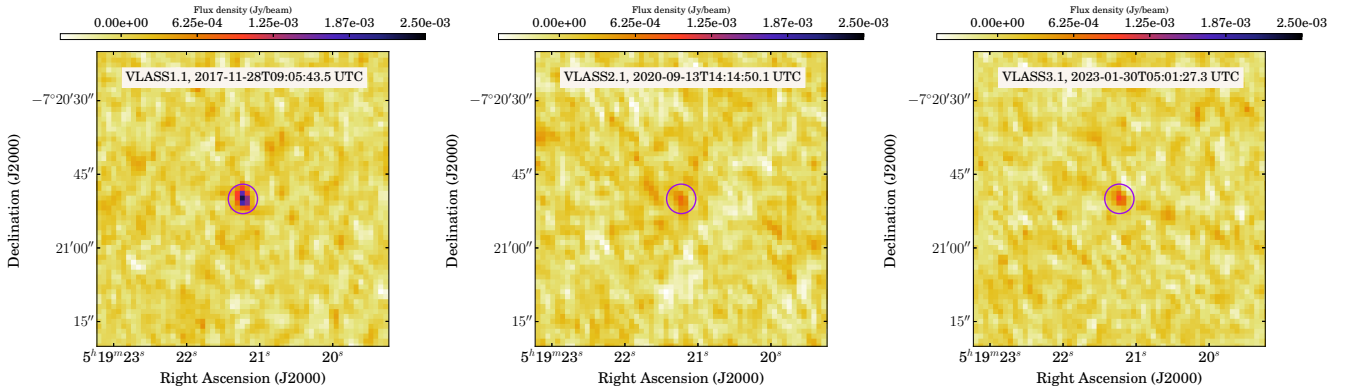


**Figure 18.** Quick look images of the sky area containing HD 34736 extracted from the Very Large Array Sky Survey (VLASS) archive. A circle with radius  $r = 6''$  is centred at the location of the star.

detection. However, an X-ray source 2SXPS J051921.1–072047 in the area of HD 34736 was detected by the X-ray Telescope (XRT) onboard the Neil Gehrels *Swift* Observatory in 2014. During 2.8 ks of exposure, in the range of 0.3–10 keV, the mean registered count rate was  $0.121 \text{ cts s}^{-1}$  (Evans et al. 2020) corresponding to a mean luminosity  $\log L_X = 29.6$  [erg  $\text{s}^{-1}$ ].

Recently, Merloni et al. (2024) released the first version of the all-sky X-ray survey eRASS in the western Galactic hemisphere, made with the extended ROentgen Survey with an Imaging Telescope Array (*eROSITA*, Predehl et al. 2021) onboard the “Spectrum-Röntgen-Gamma” (*SRG*) space observatory in the energy range 0.2–8 keV. According to the data from *eROSITA*, an X-ray source 1eRASS J051921.0–072049 with coordinates coinciding with the position of HD 34736 produced 0.268 counts per second in the range 0.2–2.3 keV (soft X-ray) and was practically inactive beyond 2.3 keV. The X-ray flux density of 1eRASS J051921.0–072049 was estimated as  $2.495 \times 10^{-13} \text{ erg s}^{-1} \text{ cm}^{-2}$ . Therefore, the logarithm of the X-ray luminosity ( $\log L_X$ ) measured in  $\text{erg s}^{-1}$  equals 30.62, consistent with that published by Grillo et al. (1992). Such values imply that HD 34736 is one of the strongest X-ray emitters among CP stars.

To study the stability of the X-ray emission of HD 34736 we have performed a custom analysis of data from the *eROSITA* archive with the use of the task `srctool` of the *eROSITA* Science Analysis Software System (eSASS, Brunner et al. 2022). For X-ray photometry, we set the radius of the object aperture to 30 arcsec; the background is evaluated within the annulus with radii 90 and 150 arcsec. The X-ray light curve in the range of energies  $\sim 0.2$ –10 keV is shown in Fig. 19. The error bars are evaluated using the Bayesian excess variances implemented in `bexvar` (Buchner et al. 2022).

The length of continuous observations of HD 34736 with *eROSITA* is shorter than the period  $P_{1A} = 1^{\text{d}}.2799885$  of the hotter magnetic component but is still sufficient to search for variation of the X-ray emission on timescales comparable to the period  $P_{1B} = 0^{\text{d}}.5226938$  of the cooler secondary component. To our surprise, the best fit of the X-ray data suggests a period  $P_X \approx 0.48$  days, which is even shorter than  $P_{1B}$ , but the amplitude of this variation is inconclusively small.

## 4 DISCUSSION AND CONCLUSIONS

Based on the results presented above, one can draw a rather comprehensive picture of the stellar system HD 34736. In some elements such as the physical parameters of the magnetic component, this picture inherits the conclusions of Paper I. But it is only with new ded-

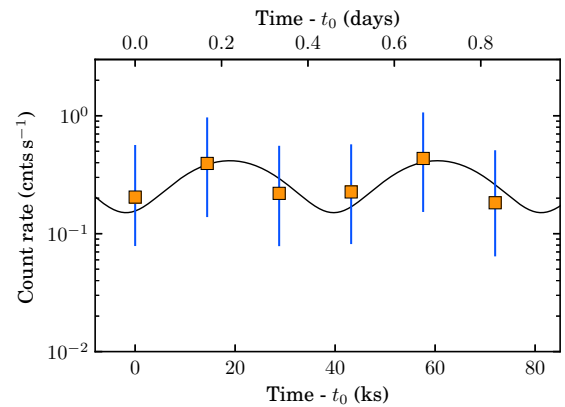


**Figure 19.** The X-ray light curve of HD 34736 in the range of  $\sim 0.2$ –10 keV. The proposed period of variation  $P_X$  is  $0^{\text{d}}.48$  (solid line).

icated spectroscopic and photometric observations that it becomes possible to uncover the intricate nature of HD 34736. In this section, we summarise the main outcomes of our research and attempt to place them in the context of modern knowledge about magnetic CP stars.

### 4.1 The double-lined binary system of HD 34736

From the variable radial velocities of lines belonging to two stars observed in its spectrum, HD 34736 can be described as a stellar system comprising two early-type components. Given the effective temperature and the observed pattern of chemical anomalies, the more massive component can be classified as a CP star of the He-wk type. Notably, subtle spectral variability has probably been detected in Mg and Si lines of the cooler component.

In Sec. 3.1, we have convincingly shown that the complex lightcurve of HD 34736 obtained by *TESS* includes signals from three major contributors. Two of them are the hot visible components with individual lightcurves typical for CP stars. The rotational period of the hotter primary star  $P_{1A}$  is 1.2799885 days, while the secondary component rotates much faster with  $P_{1B} = 0.5226938$  days. We have found that these values vary on the timescale of observations. Such a phenomenon is not rare in the world of magnetic CP stars (e.g. Mikulášek et al. 2011b; Mikulášek 2016; Shultz et al.



2019a; Mikulášek et al. 2022), but HD 34736 is to the best of our knowledge the only binary system with both components showing such behaviour. Even more intriguing is that while the main component is slowing down with the largest rate-of-change observed to date, the secondary star appears to be spinning up.

Magnetic fields are a remarkable feature of CP stars. Spectropolarimetry of HD 34736 shows that the directly observable magnetic field of this star varies with a rotational period  $P_{1A}$  (Table 1) and thus is attributable to the primary component. Even though the magnetic field of the secondary cannot be observed directly, in Sec. 3.2.2, we have collected a number of facts indicating the possible presence of a field in this star. With the longitudinal field  $\langle B_z \rangle$  estimated as 500 G, in the case of simple dipolar configuration, the mean surface magnetic field can reach  $\approx 1.5$  kG. Similar magnetic characteristics are demonstrated by CU Vir (Kochukhov et al. 2014), a CP star that is also known for its fast and variable rotation. Much alike to CU Vir, HD 34736 also attracts attention due to its X-ray and radio emission (Trigilio et al. 2000; Robrade et al. 2018; Das & Chandra 2021). A significant level of emission in the X-ray and radio domains found for the object of our study continues a series of similarities between these two stars. However, this phenomenon may be unrelated to these two stars.

To this moment, we have considered HD 34736 to be a double-lined binary system. Two variants of the orbital solution presented in Table 4 give projected masses  $M \sin^3 i$  that appear to be much larger than those expected given the  $T_{\text{eff}}$  of the components. In the solution based on the radial velocities derived through the modelling of Mg II line 448.1 nm, we have  $M \sin^3 i = 4.9 M_\odot$  for component A, and  $3.5 M_\odot$  for component B. However, given the average age of 4.6 Myr of Orion OB1c hosting HD 34736 (Semenko et al. 2022), from interpolating the MIST isochrones, one expects masses  $M_A \approx 3.2 M_\odot$  and  $M_B \approx 2.7 M_\odot$  if we use  $T_{\text{eff}A}$  and  $T_{\text{eff}B}$  as a reference. These temperatures correspond approximately to spectral types of B7V and B8V<sup>5</sup>. In contrast, even the lowest admissible masses from the orbital fit turn the primary into a B4V star and the secondary into a B7V star, respectively. On the assumption that the rotational axes of the components are orthogonal to the orbital plane and inclined by approximately  $70^\circ$  to the line-of-sight (Sec. 3.2.2), both components must be even more massive, implying spectral features of very hot stars which we undoubtedly would have recognised in our data. However, even a quick look at the recorded spectra reveals the features of the late B-type Si and He-wk peculiar stars, e.g. intense hydrogen Balmer and singly ionized silicon lines together with very weak to extinct lines of He I and Si III.

Apart from the SED fitting (Sec. 3.2.3), which also implies that the effective temperatures of the components are close to the spectroscopically derived values of 13 000 K and 11 500 K, an independent test of the fidelity of our results can be achieved using a simple calculation of the apparent brightness of the binary given its distance  $d \approx 372$  pc found from the GAIA parallax and the adopted interstellar extinction  $E(B - V) = 0.0248$  mag. The MIST evolutionary models calculated for the age of 4.6 Myr predict luminosity  $\log L_A/L_\odot \approx 2.3$  and absolute magnitude  $M_{V_A} \approx -0.17$  for the primary component with  $T_{\text{eff}A} = 13\,000$  K. After simple calculations, this gives an expected apparent magnitude  $V_A \approx 7.8^m$ . Similarly, for the secondary star with  $T_{\text{eff}B} = 11\,500$  K we get  $\log L_B/L_\odot \approx 2.0$ ,  $M_{V_B} \approx 0.24$ ,

and  $V_B \approx 8.2^m$ . Thus, the apparent magnitude  $V_{AB}$  of such an unresolved system is  $7.4^m$ , which is about  $0.4^m$  brighter than reported, e.g., by Kervella et al. (2022). Similar calculations allow us to rule out a potential scenario in which the two stars do have larger masses but in which have already evolved to the end of their main sequence stage so that their effective temperatures are close to 13 000 K and 11 500 K. Ignoring the inherent problems with an explanation of how such an old ( $t \gtrsim 100$  Myr) system can appear in the centre of a young association and show kinematic properties indistinguishable from the rest of the association members, this hypothesis about an advanced evolutionary status of HD 34736 would require higher luminosities. However, any attempt to increase the effective temperature or luminosity of the components will result in even brighter predicted apparent magnitudes.

At this point, we can conclude that the discrepancy between the stellar dynamical masses and spectral classification is real and can reasonably be explained in terms of higher-order multiplicity. The presence of a third, optically invisible component may also be necessary to explain the activity of HD 34736 observed in radio and X-ray domains. The levels measured for our target are commonly found in 1) Cool active stars and 2) Some, but not numerous, hot magnetic CP stars. A strong magnetic field is necessary to explain this phenomenon in both cases. We consider both scenarios to be feasible for HD 34736.

#### 4.1.1 Invisible cool active component?

The contradiction between the dynamical masses of the components and their spectral appearance found in Sec. 3.2.4 could be explained by the presence of a third body in the system. Several scenarios for the architecture of such a hierarchical triple system can be considered. If the two optically-visible components form an SB2 binary with  $P_{\text{orb}} = 83.2$  d and the third star orbits it on a wide orbit with a much longer period, we should observe a long-term trend in the systemic velocity  $\gamma$ , which is not evident in the  $V_r$  data. Moreover, in this case, the motion of the SB2 components on the inner orbit is not modified, leaving the dynamical mass problem unsolved. On the other hand, one of the two visible components can itself be a close binary, leading to a total mass exceeding that expected for its spectral type. In this case, we should observe additional modulation of  $V_r$  on a time scale shorter than  $P_{\text{orb}}$ . This is excluded for the narrow-line primary star but is not out of the question for the secondary given its broad lines and apparent spectral variability, leading to a large scatter of  $V_r$  measurements and systematic difference between Mg II and LSD  $V_r$  results. We explored the scenario where component B consists of two stars, *Ba* corresponding to the hot component visible in the spectrum and a lower mass component *Bb* (which we will call component C), producing no detectable optical spectral contribution. Assuming the orbital inclination is equal to the rotational inclination of the primary determined in Sec. 3.2.2,  $i_{\text{orb}} = i = 68^\circ$  and keeping all orbital parameters except  $K_B$  fixed to the values in Table 4, we found that the  $V_r$  semi-amplitude of the secondary must be reduced to  $\approx 73$  km s<sup>-1</sup> to yield a dynamical mass of the primary equal to  $3.2 M_\odot$  as estimated from MIST isochrones. The same estimate suggests  $2.7 M_\odot$  for the secondary, while its dynamical mass with the modified  $K_B$  is  $3.07 M_\odot$ . The difference is attributed to an invisible  $0.37 M_\odot$  component C orbiting component B. The  $V_r$  variation associated with this orbital motion ranges from a few km s<sup>-1</sup> to a few tens of km s<sup>-1</sup>, depending on the assumed orbital period. This amplitude is substantially below the width of spectral lines of component B, essentially leading to additional scatter in the  $V_r$  measurements of the broad-line component. This scenario leaves the question of why

<sup>5</sup> In the following classification, we use Eric Mamajek’s table “A Modern Mean Dwarf Stellar Color and Effective Temperature Sequence” for spectroscopic classification. [http://www.pas.rochester.edu/~emamajek/EEM\\_dwarf\\_UBVIJHK\\_colors\\_Teff.txt](http://www.pas.rochester.edu/~emamajek/EEM_dwarf_UBVIJHK_colors_Teff.txt)

this scatter leads to an apparent overestimation of the  $V_r$  amplitude of component  $B$  unanswered. It is possible that our measurement procedure is biased to phases with the largest velocity separation of the components  $A$  and  $B$ .

Given the young age of the system and given the detected radio and X-ray emission, we believe that the most probable candidate for the third component is a magnetically active and fast-rotating young stellar object (YSO) like a T Tau star.

Combined radio and X-ray emission is a common tracer of activity in a wide variety of objects. Guedel & Benz (1993) and Benz & Guedel (1994) find a universal relation, linking luminosity in two mentioned spectral domains:

$$\frac{L_X}{L_R} = \kappa \times 10^{15.5 \pm 1} [Hz], \quad (20)$$

where  $\kappa = 1$  for late-type active stars and various types of binaries with (sub)giants. For classical Algols, RS CVn and FK Com stars, the authors give  $\kappa \approx 0.17$ . T Tau stars and YSOs are significantly overluminous in the radio, and a constant  $\kappa$  for them is normally even smaller. For example, in a large-scale radio survey of the star-forming complexes in Ophiuchus, Dzib et al. (2013) find that  $\kappa = 0.03$ . Virtually the same value of  $\kappa$  has been derived for complexes in Serpens (Ortiz-León et al. 2015) and Taurus-Auriga (Dzib et al. 2015). Young objects in Orion appear overluminous in radio by up to two orders of magnitude and even more according to Kounkel et al. (2014).

Stuart & Gregory (2023) show that in YSOs of about one solar mass approaching the ZAMS, intense X-ray emission must be the sign of a strong magnetic field of very simple dipolar configuration. Through the modelling of the X-ray and radio emission in flaring T Tau stars, Waterfall et al. (2019) link the departure from the Güdel-Benz relation to the strength of the surface magnetic field  $B_s$ , which causes dramatic increase of the radio luminosity when  $B_s > 3$  kG. For HD 34736, we have  $\log L_X = 30.17$ ,  $\log L_R = 17.63$  and, consequently,  $\kappa = 0.001$ . In models by Waterfall et al. (2019), this level corresponds to the activity of a star with  $B_s \approx 5$  kG. Thus, we conclude that the radio and X-ray emission from HD 34736 can presumably be linked to a single source showing characteristics of young pre-MS objects with a rather strong surface magnetic field.

The X-ray luminosity of T Tau stars also depends on their mass. For the objects in the Orion Nebula Cluster, Preibisch et al. (2005) give a linear dependence between  $\log L_X$  and  $\log M$  expressed in solar units as  $\log L_X = 30.37(\pm 0.06) + 1.44(\pm 0.10) \log M$ . We have used this relation to estimate the mass of the unknown source of X-ray emission and have eventually come to an inconclusive result. The variable X-ray luminosity of HD 34736 (Sec. 3.3) brings us to a broad range of masses from about  $0.3M_\odot$  when  $\log L_X = 29.6$  to almost  $1.6M_\odot$  when  $\log L_X = 30.62$ . Fast rotation, common for YSOs, can also not be neglected since we have a signature of variability in the X-ray data. Different aspects of the rotation problem and its relationship to activity are discussed for the X-ray-active YSOs in several open clusters by Argiroffi et al. (2016) and Getman et al. (2023).

Additional observations may help to clarify the invisible body's evolutionary status and infer its real physical parameters.

#### 4.1.2 Or magnetospheres?

At the same time, one cannot completely rule out the possibility of magnetospheric activity in B-type components.

Magnetic early-type stars with strong surface magnetic field and rapid rotation are extremely likely to produce non-thermal radio emission (Leto et al. 2021; Shultz et al. 2022). It has been recently

shown that such emission is driven by magnetic reconnections triggered by centrifugal breakout (CBO) events (Owocki et al. 2022). CBOs are small-scale explosions in the magnetosphere during which magnetically confined stellar wind plasma breaks open the field lines temporarily and escapes the star. A necessary condition for CBOs to take place is that the Alfvén radius  $R_A$  should be larger than the Kepler radius  $R_K$  (see Ud-Doula et al. 2008, for definitions of  $R_A$  and  $R_K$ ). The region between the Kepler radius and the Alfvén radius is named the centrifugal magnetosphere (CM, Petit et al. 2013). For the stellar parameters of the magnetic primary (magnetic field strength is taken as 8.9 kG, Sec. 3.2.2), we estimate the two parameters as  $R_K = 3.6 R_*$  and  $R_A = 79 R_*$ , establishing that the star's magnetosphere should experience CBOs and can drive non-thermal radio emission. In case of the secondary star, if we assume it to have a surface magnetic field strength of  $\approx 1.5$  kG (Sec. 3.2.2), we find  $R_K = 1.8 R_*$ , and  $R_A \approx 37 R_*$ , suggesting that the secondary is also capable of producing radio emission if it is indeed magnetic.

The observed violation of the Güdel-Benz relation is actually consistent with the known properties of magnetic hot stars, where the radio and X-ray emission are primarily produced by two distinct channels. The X-ray emission is produced due to the shock resulting from the collision between magnetically channelled stellar winds from the two magnetic hemispheres (e.g. ud-Doula & Nazé 2016), whereas the radio is driven by the CBOs. In addition, hot magnetic stars have been found to be overluminous in radio with respect to the Güdel-Benz relation (Leto et al. 2017, 2018; Robrade et al. 2018). For CU Vir, the ratio between X-ray and spectral radio luminosity was found to be  $10^{12}$  Hz (Robrade et al. 2018), similar to that observed for the case of HD 34736.

Finally, the variable radio emission observed between different epochs of observation is also one of the characteristics of non-thermal radio emission observed from magnetic early-type stars. The incoherent radio emission exhibits a rotational modulation that correlates with that observed for the longitudinal magnetic field. In addition to the incoherent emission, some magnetic hot stars also produce coherent radio emission observed as periodic radio pulses (e.g. Triguero et al. 2000; Das et al. 2022), adding further variability to the lightcurve. Due to the sparse rotational phase coverage, it is unclear whether or not HD 34736 also produces coherent radio emission. Future observations around the rotational phases of enhanced flux density will be able to provide conclusive evidence in this direction.

If the secondary star is confirmed to be magnetic, there could be another source of variability, both in radio and X-ray, related to binary magnetospheric interaction. So far,  $\epsilon$  Lupi is the only magnetic hot star binary system that has been investigated for such variability, and it was found to produce enhanced X-ray and radio emission at the periastron phase (Das et al. 2023; Biswas et al. 2023). In particular, the radio lightcurve, which has a better orbital phase coverage, revealed secondary enhancements at orbital phases away from the periastron that turned out to be persistent (Biswas et al. 2023). The reason behind those enhancements is not well understood.

Thus, the combination of binarity, magnetism, variable X-ray, and radio emission make HD 34736 an important system for follow-up observation in both radio and X-ray wavebands in order to pinpoint the true origin of the emission and their significance for the stellar system itself.

## 4.2 Concluding remarks

The results obtained in our ten-year-long study of HD 34736 and presented in this paper potentially put this star in a special place among known binary and multiple systems with magnetic components. Not

only does the young age and strong magnetic field of the primary make HD 34736 unique, but it is its unprecedented combination of components on different stages of stellar evolution. Here, we have two MS stars, which just entered the ZAMS or are approaching it, and a potential T Tau-like object. Apart from the main component, where the magnetic field is firmly detected using spectropolarimetry, we have indirect evidence of magnetic fields in two other companions. Only three binary systems comprising two components with firmly detected magnetic fields are known to date. Two pairs, namely HD 156424 (Shultz et al. 2021) and BD +40° 175 (El'kin 1999; Semenko et al. 2011), belong to wide systems with orbital periods order of years and decades. In this list, the doubly-magnetic  $\epsilon$  Lup (Shultz et al. 2015) is the only system with an orbital period shorter than a year. The formation and evolution of compact magnetic binaries can be used to validate hypotheses explaining the origin of stellar magnetism in the upper main sequence of the Hertzsprung-Russell diagram. Explaining the case of HD 34736 with more than two magnetic components, it is reasonable to conclude that the magnetic properties of the protostellar environment and the mechanisms of evolution other than stellar mergers (as in the case of some known magnetic hot stars, e.g. the case of HD 148937, Frost et al. 2024) are responsible for the appearance of at least some multiple magnetic systems.

## ACKNOWLEDGMENTS

The authors express their gratitude to the anonymous reviewer for their insightful suggestions and comments.

D.S. acknowledges financial support from the project PID2021-126365NB-C21(MCI/AEI/FEDER, UE) and from the Severo Ochoa grant CEX2021-001131-S funded by MCIN/AEI/10.13039/501100011033.

E.A. acknowledges support by the “Programme National de Physique Stellaire” (PNPS) of CNRS/INSU co-funded by CEA and CNES.

I.Y. is grateful to the Russian Foundations for Basic Research for financial support (grant no. 19-32-60007).

O.K. acknowledges support from the Swedish Research Council (projects 2019-03548 and 2023-03667), the Swedish National Space Board (projects 185/14, 137/17), and the Royal Swedish Academy of Sciences.

Z.M. & J.J. are grateful that publication could produced within the framework of institutional support for the development of the research organization of Masaryk University.

G.A.W acknowledges Discovery Grant support from the Natural Sciences and Engineering Research Council (NSERC) of Canada.

The research leading to these results has (partially) received funding from the KU Leuven Research Council (grant C16/18/005: PARADISE), from the Research Foundation Flanders (FWO) under grant agreement G089422N, as well as from the BELgian federal Science Policy Office (BELSPO) through PRODEX grant PLATO.

The research was partially supported by the grant 21-12-00147 (Russian Science Foundation).

This work is partially based on observations obtained at the Canada-France-Hawaii Telescope (CFHT), which is operated by the National Research Council of Canada, the Institut National des Sciences de l'Univers (INSU) of the Centre National de la Recherche Scientifique of France, and the University of Hawaii. Observations with the 6-m telescope BTA of the Special Astrophysical Observatory are supported by the Ministry of Science and Higher Education

of the Russian Federation. This work has used the VALD, NASA ADS, and SIMBAD databases.

This paper includes data collected by the *TESS* mission, publicly available from the Mikulski Archive for Space Telescopes (MAST). Funding for the *TESS* mission is provided by the NASA's Science Mission Directorate. This project makes use of data from the KELT survey, including support from The Ohio State University, Vanderbilt University, and Lehigh University.

This work is based on data from *eROSITA*, the soft X-ray instrument aboard SRG, a joint Russian-German science mission supported by the Russian Space Agency (Roskosmos), in the interests of the Russian Academy of Sciences represented by its Space Research Institute (IKI), and the Deutsches Zentrum für Luft- und Raumfahrt (DLR). The *SRG* spacecraft was built by Lavochkin Association (NPOL) and its subcontractors, and is operated by NPOL with support from the Max Planck Institute for Extraterrestrial Physics (MPE). The development and construction of the *eROSITA* X-ray instrument was led by MPE, with contributions from the Dr. Karl Remeis Observatory Bamberg & ECAP (FAU Erlangen-Nuernberg), the University of Hamburg Observatory, the Leibniz Institute for Astrophysics Potsdam (AIP), and the Institute for Astronomy and Astrophysics of the University of Tübingen, with the support of DLR and the Max Planck Society. The Argelander Institute for Astronomy of the University of Bonn and the Ludwig Maximilians Universität Munich also participated in the science preparation for *eROSITA*. The *eROSITA* data shown here were processed using the eSASS software system developed by the German *eROSITA* consortium.

## DATA AVAILABILITY

The authors can provide the extracted 1D spectra and light curves used in this study upon a reasonable request.

## REFERENCES

- Alecian E., et al., 2015, in Meynet G., Georgy C., Groh J., Stee P., eds, IAU Symposium Vol. 307, New Windows on Massive Stars. pp 330–335 ([arXiv:1409.1094](https://arxiv.org/abs/1409.1094)), doi:10.1017/S1743921314007030
- Amôres E. B., Lépine J. R. D., 2005, *AJ*, **130**, 659
- Argiroffi C., Caramazza M., Micela G., Sciortino S., Moraux E., Bouvier J., Flaccomio E., 2016, *A&A*, **589**, A113
- Asplund M., Amarsi A. M., Grevesse N., 2021, *A&A*, **653**, A141
- Aurière M., et al., 2007, *A&A*, **475**, 1053
- Bailey J. D., Landstreet J. D., 2013, *Astronomy and Astrophysics*, **551**, A30
- Benz A. O., Guedel M., 1994, *A&A*, **285**, 621
- Biswas A., et al., 2023, *MNRAS*, **523**, 5155
- Borkovits T., Hajdu T., Sztakovics J., Rappaport S., Levine A., Bíró I. B., Klagyivik P., 2016, *MNRAS*, **455**, 4136
- Brown A. G. A., de Geus E. J., de Zeeuw P. T., 1994, *A&A*, **289**, 101
- Brunner H., et al., 2022, *A&A*, **661**, A1
- Buchner J., Boller T., Bogensberger D., Malyali A., Nandra K., Wilms J., Dwelly T., Liu T., 2022, *A&A*, **661**, A18
- Choi J., Dotter A., Conroy C., Cantiello M., Paxton B., Johnson B. D., 2016, *ApJ*, **823**, 102
- Cohen M., Wheaton W. A., Megeath S. T., 2003, *AJ*, **126**, 1090
- Condon J. J., Cotton W. D., Greisen E. W., Yin Q. F., Perley R. A., Taylor G. B., Broderick J. J., 1998, *AJ*, **115**, 1693
- Cutri R. M., et al., 2003, 2MASS All Sky Catalog of point sources.
- Das B., Chandra P., 2021, *ApJ*, **921**, 9
- Das B., et al., 2022, *ApJ*, **925**, 125
- Das B., et al., 2023, *MNRAS*, **522**, 5805

- Donati J. F., 2003, in Trujillo-Bueno J., Sanchez Almeida J., eds, *Astronomical Society of the Pacific Conference Series Vol. 307, Solar Polarization*. p. 41
- Donati J. F., Semel M., Carter B. D., Rees D. E., Collier Cameron A., 1997, *MNRAS*, **291**, 658
- Dotter A., 2016, *ApJS*, **222**, 8
- Dzib S. A., et al., 2013, *ApJ*, **775**, 63
- Dzib S. A., et al., 2015, *ApJ*, **801**, 91
- El'kin V. G., 1999, *Astronomy Letters*, **25**, 809
- Evans P. A., et al., 2020, *ApJS*, **247**, 54
- Frost A. J., et al., 2024, *Science*, **384**, 214
- Gaia Collaboration 2022, *VizieR Online Data Catalog*, p. I/355
- Gaia Collaboration et al., 2022, arXiv e-prints, p. arXiv:2208.00211
- Getman K. V., Feigelson E. D., Garmire G. P., 2023, *ApJ*, **952**, 63
- Gray D. F., 2008, *The Observation and Analysis of Stellar Photospheres*
- Grillo F., Sciortino S., Micela G., Vaiana G. S., Harnden F. R. J., 1992, *ApJS*, **81**, 795
- Guedel M., Benz A. O., 1993, *ApJ*, **405**, L63
- Hackman T., Lehtinen J., Rosén L., Kochukhov O., Käpylä M. J., 2016, *A&A*, **587**, A28
- Hartman J., 2012, *VARTOOLS: Light Curve Analysis Program*, *Astrophysics Source Code Library* (ascl:1208.016)
- Heiter U., et al., 2002, *A&A*, **392**, 619
- Hubrig S., et al., 2005, *A&A*, **440**, L37
- Iglesias-Marzoa R., López-Morales M., Jesús Arévalo Morales M., 2015, *Publications of the Astronomical Society of the Pacific*, **127**, 567
- Jermyn A. S., Cantiello M., 2020, *ApJ*, **900**, 113
- Jouve L., Lignières F., Gaurat M., 2020, *A&A*, **641**, A13
- Kervella P., Arenou F., Thévenin F., 2022, *A&A*, **657**, A7
- Keszthelyi Z., Meynet G., Georgy C., Wade G. A., Petit V., David-Uraz A., 2019, *MNRAS*, **485**, 5843
- Khan S. A., Shulyak D. V., 2006, *A&A*, **454**, 933
- Kochukhov O. P., 2007, in Romanyuk I. I., Kudryavtsev D. O., Neizvestnaya O. M., Shapoval V. M., eds, *Physics of Magnetic Stars*. pp 109–118 (arXiv:astro-ph/0701084)
- Kochukhov O., 2016, in Rozelot J.-P., Neiner C., eds, , Vol. 914, *Lecture Notes in Physics*, Berlin Springer Verlag. p. 177, doi:10.1007/978-3-319-24151-7\_9
- Kochukhov O., 2018, *Contributions of the Astronomical Observatory Skalnaté Pleso*, **48**, 58
- Kochukhov O., Shulyak D., 2019, *ApJ*, **873**, 69
- Kochukhov O., Drake N. A., Piskunov N., de la Reza R., 2004, *A&A*, **424**, 935
- Kochukhov O., Makaganiuk V., Piskunov N., 2010, *A&A*, **524**, A5
- Kochukhov O., Lüftinger T., Neiner C., Alecian E., MiMeS Collaboration 2014, *A&A*, **565**, A83
- Kochukhov O., Silvester J., Bailey J. D., Land street J. D., Wade G. A., 2017, *A&A*, **605**, A13
- Kochukhov O., Shultz M., Neiner C., 2019, *A&A*, **621**, A47
- Kochukhov O., Gürsoytrak Mutlay H., Amarsi A. M., Petit P., Mutlay I., Gürol B., 2023, *MNRAS*, **521**, 3480
- Kounkel M., et al., 2014, *ApJ*, **790**, 49
- Kovács G., Bakos G., Noyes R. W., 2005, *MNRAS*, **356**, 557
- Krtićka J., et al., 2019, *A&A*, **625**, A34
- Krtićka J., Mikulášek Z., Kurfürst P., Oksala M. E., 2022, *A&A*, **659**, A37
- Kupka F., Piskunov N., Ryabchikova T. A., Stempels H. C., Weiss W. W., 1999, *A&AS*, **138**, 119
- Lacy M., et al., 2020, *PASP*, **132**, 035001
- Landstreet J. D., Bagnulo S., Andretta V., Fossati L., Mason E., Silaj J., Wade G. A., 2007, *A&A*, **470**, 685
- Leone F., Manfre M., 1997, *A&A*, **320**, 257
- Leto P., et al., 2017, *MNRAS*, **467**, 2820
- Leto P., et al., 2018, *MNRAS*, **476**, 562
- Leto P., et al., 2021, *MNRAS*, **507**, 1979
- Lignières F., Petit P., Aurière M., Wade G. A., Böhm T., 2014, in Petit P., Jardine M., Spruit H. C., eds, *IAU Symposium Vol. 302, Magnetic Fields throughout Stellar Evolution*. pp 338–347 (arXiv:1402.5362), doi:10.1017/S1743921314002440
- McMullin J. P., Waters B., Schiebel D., Young W., Golap K., 2007, in Shaw R. A., Hill F., Bell D. J., eds, *Astronomical Society of the Pacific Conference Series Vol. 376, Astronomical Data Analysis Software and Systems XVI*. p. 127
- Merloni A., et al., 2024, *A&A*, **682**, A34
- Meynet G., Eggenberger P., Maeder A., 2011, *A&A*, **525**, L11
- Michaud G., 1970, *ApJ*, **160**, 641
- Michaud G., Alecian G., Richer J., 2015, *Atomic Diffusion in Stars*, doi:10.1007/978-3-319-19854-5.
- Mikulasek Z., et al., 2021, in *OBA Stars: Variability and Magnetic Fields*. p. 17, doi:10.5281/zenodo.5040838
- Mikulášek Z., 2016, *Contributions of the Astronomical Observatory Skalnaté Pleso*, **46**, 95
- Mikulášek Z., Wolf M., Zejda M., Pecharová P., 2006, *Ap&SS*, **304**, 363
- Mikulášek Z., et al., 2008, *A&A*, **485**, 585
- Mikulášek Z., Zejda M., Qian S., Zhu L., 2011a, in Qian S., Leung K., Zhu L., Kwok S., eds, *Astronomical Society of the Pacific Conference Series Vol. 451, 9th Pacific Rim Conference on Stellar Astrophysics*. p. 111
- Mikulášek Z., et al., 2011b, *A&A*, **534**, L5
- Mikulášek Z., Zejda M., Janík J., 2012, in Richards M. T., Hubeny I., eds, *Vol. 282, From Interacting Binaries to Exoplanets: Essential Modeling Tools*. pp 391–394, doi:10.1017/S1743921311027888
- Mikulášek Z., et al., 2020, in Wade G., Alecian E., Bohlender D., Sigut A., eds, *Vol. 11, Stellar Magnetism: A Workshop in Honour of the Career and Contributions of John D. Landstreet*. pp 46–53 (arXiv:1912.04121), doi:10.48550/arXiv.1912.04121
- Mikulášek Z., Semenko E., Paunzen E., Hümmerich S., North P. L., Bernhard K., Krtićka J., Janík J., 2022, *A&A*, **668**, A159
- Monin D., Bohlender D., Hardy T., Saddlemyer L., Fletcher M., 2012, *PASP*, **124**, 329
- Monteiro G., Guerrero G., Del Sordo F., Bonanno A., Smolarkiewicz P. K., 2023, *MNRAS*, **521**, 1415
- Morgan D. H., Nandy K., Thompson G. L., 1978, *MNRAS*, **185**, 371
- Moss D., 1989, *MNRAS*, **236**, 629
- Oksala M. E., Silvester J., Kochukhov O., Neiner C., Wade G. A., MiMeS Collaboration 2018, *MNRAS*, **473**, 3367
- Ortiz-León G. N., et al., 2015, *ApJ*, **805**, 9
- Owoccki S. P., Shultz M. E., ud-Doula A., Chandra P., Das B., Leto P., 2022, *MNRAS*, **513**, 1449
- Pakhomov Y. V., Ryabchikova T. A., Piskunov N. E., 2019, *Astronomy Reports*, **63**, 1010
- Panchuk V. E., Chuntunov G. A., Naidenov I. D., 2014, *Astrophysical Bulletin*, **69**, 339
- Pepper J., et al., 2007, *PASP*, **119**, 923
- Pepper J., Kuhn R. B., Siverd R., James D., Stassun K., 2012, *PASP*, **124**, 230
- Petit V., et al., 2013, *MNRAS*, **429**, 398
- Piskunov N. E., Kupka F., Ryabchikova T. A., Weiss W. W., Jeffery C. S., 1995, *A&AS*, **112**, 525
- Predehl P., et al., 2021, *A&A*, **647**, A1
- Preibisch T., et al., 2005, *ApJS*, **160**, 401
- Preston G. W., 1967, *ApJ*, **150**, 547
- Preston G. W., 1974, *ARA&A*, **12**, 257
- Raskin G., et al., 2011, *A&A*, **526**, A69
- Renson P., Manfroid J., 2009, *Astronomy and Astrophysics*, **498**, 961
- Ricker G. R., et al., 2014, in Oschmann Jacobus M. J., Clampin M., Fazio G. G., MacEwen H. A., eds, *Society of Photo-Optical Instrumentation Engineers (SPIE) Conference Series Vol. 9143, Space Telescopes and Instrumentation 2014: Optical, Infrared, and Millimeter Wave*. p. 914320 (arXiv:1406.0151), doi:10.1117/12.2063489
- Robrade J., Oskinoval L. M., Schmitt J. H. M. M., Leto P., Trigilio C., 2018, *A&A*, **619**, A33
- Roman N. G., 1978, *AJ*, **83**, 172
- Romanovskaya A., Ryabchikova T., Shulyak D., Perraut K., Valyavin G., Burlakova T., Galazutdinov G., 2019, *MNRAS*, **488**, 2343
- Romanovskaya A. M., Shulyak D. V., Ryabchikova T. A., Sitnova T. M., 2021, *A&A*, **655**, A106
- Romanyuk I. I., Semenko E. A., Yakunin I. A., Kudryavtsev D. O., 2013, *Astrophysical Bulletin*, **68**, 300

- Romanyuk I. I., Semenko E. A., Yakunin I. A., Kudryavtsev D. O., 2017, in Balega Y. Y., Kudryavtsev D. O., Romanyuk I. I., Yakunin I. A., eds, *Astronomical Society of the Pacific Conference Series* Vol. 510, *Stars: From Collapse to Collapse*. p. 214
- Romanyuk I. I., Semenko E. A., Moiseeva A. V., Yakunin I. A., Kudryavtsev D. O., 2019, *Astrophysical Bulletin*, **74**, 55
- Romanyuk I. I., Semenko E. A., Moiseeva A. V., Yakunin I. A., Kudryavtsev D. O., 2021a, *Astrophysical Bulletin*, **76**, 39
- Romanyuk I. I., Semenko E. A., Moiseeva A. V., Yakunin I. A., Kudryavtsev D. O., 2021b, *Astrophysical Bulletin*, **76**, 163
- Rosén L., Kochukhov O., Hackman T., Lehtinen J., 2016, *A&A*, **593**, A35
- Rusomarov N., Kochukhov O., Ryabchikova T., Ilyin I., 2016, *A&A*, **588**, A138
- Ryabchikova T., et al., 2006, *A&A*, **445**, L47
- Ryabchikova T., Piskunov N., Kurucz R. L., Stempels H. C., Heiter U., Pakhomov Y., Barklem P. S., 2015, *Phys. Scr.*, **90**, 054005
- Schneider F. R. N., Ohlmann S. T., Podsiadlowski P., Röpké F. K., Balbus S. A., Pakmor R., Springel V., 2019, *Nature*, **574**, 211
- Semenko E., 2020, in *European Physical Journal Web of Conferences*. p. 05003, doi:10.1051/epjconf/202024005003
- Semenko E. A., Kichigina L. A., Kuchaeva E. Y., 2011, *Astronomische Nachrichten*, **332**, 948
- Semenko E. A., Romanyuk I. I., Kudryavtsev D. O., Yakunin I. A., 2014, *Astrophysical Bulletin*, **69**, 191
- Semenko E., Romanyuk I., Yakunin I., Kudryavtsev D., Moiseeva A., 2022, *MNRAS*, **515**, 998
- Shorlin S. L. S., Wade G. A., Donati J. F., Landstreet J. D., Petit P., Sigut T. A. A., Strasser S., 2002, *A&A*, **392**, 637
- Shultz M., Wade G. A., Alecian E., BinaMiCS Collaboration 2015, *MNRAS*, **454**, L1
- Shultz M., Rivinius T., Das B., Wade G. A., Chandra P., 2019a, *MNRAS*, **486**, 5558
- Shultz M. E., et al., 2019b, *MNRAS*, **490**, 274
- Shultz M. E., Rivinius T., Wade G. A., Kochukhov O., Alecian E., David-Uraz A., Sikora J., 2021, *MNRAS*, **504**, 4850
- Shultz M. E., et al., 2022, *MNRAS*, **513**, 1429
- Shulyak D., Tsymbal V., Ryabchikova T., Stütz C., Weiss W. W., 2004, *A&A*, **428**, 993
- Shulyak D., Kochukhov O., Khan S., 2008, *A&A*, **487**, 689
- Shulyak D., Ryabchikova T., Kochukhov O., 2013, *A&A*, **551**, A14
- Sikora J., Wade G. A., Power J., Neiner C., 2019a, *MNRAS*, **483**, 2300
- Sikora J., Wade G. A., Power J., Neiner C., 2019b, *MNRAS*, **483**, 3127
- Silvester J., Wade G. A., Kochukhov O., Bagnulo S., Folsom C. P., Hanes D., 2012, *MNRAS*, **426**, 1003
- Stibbs D. W. N., 1950, *MNRAS*, **110**, 395
- Stuart K. A., Gregory S. G., 2023, *MNRAS*, **525**, 4243
- Trigilio C., Leto P., Leone F., Umama G., Buemi C., 2000, *A&A*, **362**, 281
- Ud-Doula A., Owocki S. P., Townsend R. H. D., 2008, *MNRAS*, **385**, 97
- Wade G. A., Donati J. F., Landstreet J. D., Shorlin S. L. S., 2000, *Monthly Notices of the Royal Astronomical Society*, **313**, 851
- Waterfall C. O. G., Browning P. K., Fuller G. A., Gordovskyy M., 2019, *MNRAS*, **483**, 917
- ud-Doula A., Nazé Y., 2016, *Advances in Space Research*, **58**, 680

## APPENDIX A: PHENOMENOLOGICAL MODEL OF A ROTATIONALLY MODULATED VARIABLE

### A1 Models of phase function

The following semi-phenomenological analysis aims to model as accurately as possible the observed photometric variations of the HD 34736 object in the KELT and *TESS* filters and to derive the rotation periods of the outer co-rotating layers of both components of the binary star so that it is possible to describe and discuss both the distribution and parameters of the photometric and spectroscopic spots, as well as the geometry of magnetic fields (if any). From long-term observations of well-monitored mCP stars, it follows that the phase curves of photometric, spectroscopic, and spectropolarimetric measurements are unchanged in the time scale of decades or centuries; it is advantageous to introduce and use the concept of a monotonically raising *phase function*  $\vartheta(t)$ , which is the sum of an epoch  $E(t)$  and a common phase  $\varphi(t)$ ,  $\vartheta(t) = E(t) + \varphi(t)$  in further studies. The phase function  $\vartheta(t)$  and its inversion time-like function  $\Theta(\vartheta)$  are related to an instantaneous period  $P(t)$  (or  $P(\vartheta)$ ) through simple differential equations with a boundary condition (for details see in Mikulášek et al. 2008; Mikulášek 2016):

$$\frac{d\vartheta}{dt} = \frac{1}{P(t)}; \quad \vartheta(t = M_0) = 0; \quad \Rightarrow \quad \vartheta(t) = \int_{M_0}^t \frac{d\tau}{P(\tau)}; \quad (\text{A1})$$

$$\frac{d\Theta(\vartheta)}{d\vartheta} = P(\vartheta); \quad \Theta(0) = M_0; \quad \Theta(\vartheta) = M_0 + \int_0^{\vartheta} P(\zeta) d\zeta, \quad (\text{A2})$$

where  $\tau$  and  $\zeta$  are auxiliary variables. Using  $\Theta(\vartheta)$ , we can predict the moment of the zero-th phases  $t(\varphi = 0, E) = \Theta(E)$  for a chosen epoch  $E$ . The common phase  $\varphi(\vartheta)$  and the epoch  $E(\vartheta)$  for a chosen phase function  $\vartheta(t)$  are given by the relations:  $\varphi(t) = \text{FP}(\vartheta(t))$  and  $E = \text{IP}(\vartheta)$ , where FP and IP are the operators for the fractional part and the integer part of a number.

It is useful to introduce an auxiliary variable  $\vartheta_0(t)$  instead of time

$$\vartheta_0(t) = \frac{t - M_0}{P_0}, \quad (\text{A3})$$

where  $P_0$  is the instantaneous period at the properly chosen origin of epoch counting at the  $t = M_0$ . Then

$$\frac{d\vartheta(\vartheta_0)}{d\vartheta_0} = \frac{P_0}{P(\vartheta_0)}; \quad \frac{d\vartheta_0(\vartheta)}{d\vartheta} = \frac{P(\vartheta)}{P_0}; \quad (\text{A4})$$

$$\vartheta(\vartheta_0) = \int_0^{\vartheta_0} \frac{P_0}{P(\vartheta'_0)} d\vartheta'_0; \quad \vartheta_0(\vartheta) = \int_0^{\vartheta} \frac{P(\vartheta')}{P_0} d\vartheta'. \quad (\text{A5})$$

### A2 Linear Maclaurin and orthogonal phase function model

Period analysis of mCP stars show that the rotational periods of the majority of them are constant (Mikulášek 2016) which means that the solutions of the eqs. (A1) and (A2) for the phase function  $\vartheta(t)$  and its inversion  $\Theta(\vartheta)$  are linear and the same as the auxiliary variable  $\vartheta_0$  introduced above (A3)

$$P(t) = P_1; \quad \vartheta(t) = \vartheta_0(t) = \frac{t - M_0}{P_1}; \quad t(\vartheta) = M_0 + P_1 \vartheta, \quad (\text{A6})$$

with only two parameters of the linear ephemeris: the mean period  $P_1$  is the BJD time of one, selected primary maximum of the observed light curve. We can this form of the ephemeris transform into the

orthogonal form as:

$$\Theta(\vartheta) = (M_0 + \eta_1 P_1) + P_1(\vartheta - \eta_1) = M_1 + P_1(\vartheta - \eta_1); \quad (\text{A7})$$

$$\eta_1 = \text{round}\left(\frac{\sum \vartheta_i w_i}{\sum w_i}\right); \quad M_1 = M_0 + \eta_1 P_1, \quad \vartheta_1(t) = \frac{t - M_1}{P_1},$$

where  $w_i$  are weights of individual measurements,  $\vartheta_1(t)$  is an orthogonal form of linear phase function. Knowing the uncertainties of orthogonal parameters of linear approximation  $\delta M_1, \delta P_1$  we can easily estimate uncertainties of quantities  $\delta\Theta(\vartheta)$  and  $\delta\vartheta(t)$ .

$$\delta\Theta(\vartheta) = \sqrt{(\delta M_1)^2 + [\delta P_1(\vartheta - \eta_1)]^2}, \quad \delta\vartheta(t) = \delta\Theta(\vartheta)/P_1. \quad (\text{A8})$$

### A3 Quadratic Maclaurin and orthogonal phase function model

Let us now assume that the instantaneous period  $P(t)$  at a moment  $t$  varies in a linear way such that

$$P(t) = P_0 + \dot{P}(t - M_0) = P_0(1 + \dot{P}\vartheta_0); \quad \text{where } \vartheta_0 = \frac{t - M_0}{P_0}. \quad (\text{A9})$$

Then using equations in (A5) we obtain the phase function:

$$\vartheta(\vartheta_0) = \int_0^{\vartheta_0} \frac{d\vartheta'_0}{1 + \dot{P}\vartheta'_0} = \frac{\ln(1 + \dot{P}\vartheta_0)}{\dot{P}} \simeq \vartheta_0 - \frac{1}{2}\dot{P}\vartheta_0^2, \quad (\text{A10})$$

which we truncate to the two first term as  $\dot{P}$  is generally very small in our context. Now we can isolate the time phase function  $\vartheta_0$  by the equation A10 and expanding the exponential in a series. Using Eq. A4 we can calculate the instant period  $P(\vartheta)$  as a function of the phase function  $\vartheta$ :

$$\vartheta_0(\vartheta) = \frac{e^{\dot{P}\vartheta} - 1}{\dot{P}} \simeq \vartheta + \frac{\dot{P}}{2}\vartheta^2, \quad (\text{A11})$$

$$P(\vartheta) = P_0 \frac{d\vartheta_0}{d\vartheta} = P_0 e^{\dot{P}\vartheta} \simeq P_0(1 + \dot{P}\vartheta), \quad (\text{A12})$$

$$\Theta(\vartheta) = M_0 + P_0\vartheta_0 \simeq M_0 + P_0\vartheta + \frac{P_0\dot{P}\vartheta^2}{2}. \quad (\text{A13})$$

A disadvantage of the Maclaurin ephemeris model described by relation is the correlation between ephemeris parameters that hinders the error analysis. Mathematically, the model represented by the simplified equation A13 is a simple quadratic polynomial with respect  $\vartheta$ . This allows us to construct an orthogonal version of the phase function model (for details see in Mikulášek et al. 2008; Mikulášek 2016), allowing for a more robust error estimation, using the standard Gram-Schmidt procedure, as follow:

$$\begin{aligned} \Theta(\vartheta) &\simeq M_1 + P_1(\vartheta - \eta_1) + \frac{P'P_1}{2}(\vartheta^2 - \eta_{21}\vartheta - \eta_{20}) = \\ &= M_1 + P_1(\vartheta - \eta_1) + \frac{P'P_1}{2}(\vartheta - \eta_2)(\vartheta - \eta_3), \end{aligned} \quad (\text{A14})$$

where  $M_1, P_1$ , and  $P'$  are parameters of the orthogonal square ephemeris. The orthogonalization coefficients  $\eta_1, \eta_2, \eta_3, \eta_{20}$ , and  $\eta_{21}$  were opted so they fulfill the following orthogonalization constraints:

$$\begin{aligned} \overline{(\vartheta - \eta_1)} &= \overline{\vartheta^2 - \eta_{21}\vartheta - \eta_{20}} = \overline{\vartheta(\vartheta - \eta_2)(\vartheta - \eta_3)(\vartheta - \eta_1)} = 0; \\ \overline{\vartheta(\vartheta^2 - \eta_{21}\vartheta - \eta_{20})} &= \overline{\vartheta(\vartheta - \eta_2)(\vartheta - \eta_3)} = 0; \end{aligned} \quad (\text{A15})$$

$$\overline{\vartheta^q} = \frac{\sum \vartheta_i^q w_i}{\sum w_i}, \quad \eta_{21} = \frac{\overline{\vartheta^3} - \overline{\vartheta^2}\overline{\vartheta}}{\overline{\vartheta^2} - \overline{\vartheta}^2}; \quad \eta_{20} = \frac{\overline{\vartheta^2} - \overline{\vartheta}^2}{\overline{\vartheta^2} - \overline{\vartheta}^2};$$

$$\begin{aligned} \eta_1 &= \text{round}(\overline{\vartheta}); \quad \eta_{3,2} = \frac{\eta_{21}}{2} \pm \sqrt{\left(\frac{\eta_{21}}{2}\right)^2 + \eta_{20}}, \\ \eta_{20} &= -\eta_2\eta_3; \quad \eta_{21} = \eta_2 + \eta_3. \end{aligned} \quad (\text{A16})$$

Using this ephemeris form (A14) in our model fitting, we obtain the values of the parameters  $M_1, P_1$ , and  $P'$ , including their uncorrelated uncertainties.

If we set  $\vartheta = E$ , where  $E$  is an integer epoch, in the equation (A14), we obtain the moment of the zero phase  $\varphi$  for this epoch.

$$\begin{aligned} \Theta(E) &\simeq M_1 + P_1(E - \eta_1) + \frac{P'P_1}{2}(E^2 - \eta_{21}E - \eta_{20}) = \\ &= M_1 + P_1(E - \eta_1) + \frac{P'P_1}{2}(E - \eta_2)(E - \eta_3). \end{aligned} \quad (\text{A17})$$

The instantaneous periods for the phase function  $\vartheta$ , or the epoch  $E$ ,  $P(\vartheta), P(E)$ , equal to:

$$P(\vartheta) = \frac{dt}{d\vartheta} = P_1 + P'P_1\left(\vartheta - \frac{\eta_{21}}{2}\right); \quad P(E) = P(\vartheta = E). \quad (\text{A18})$$

Introducing time-like quantity  $\vartheta_1(t)$  we can compute the phase function  $\vartheta(t)$  and the instantaneous period  $P(t)$  for any moment  $t$

$$\vartheta_1 = \frac{t - M_1}{P_1} + \eta_1; \quad \vartheta(\vartheta_1) = \vartheta_1 - \frac{P'}{2}(\vartheta_1^2 - \eta_{21}\vartheta_1 - \eta_{20}), \quad (\text{A19})$$

$$P(t) = P_1 \frac{d\vartheta_1}{d\vartheta} = \frac{P_1}{1 - P'(\vartheta_1 - \frac{\eta_{21}}{2})} \simeq P_1 \left[1 + P' \left(\vartheta_1 - \frac{\eta_{21}}{2}\right)\right]; \quad (\text{A20})$$

$$\dot{P}(t) = \frac{1}{P_1} \frac{dP}{d\vartheta_1} = P' = \dot{P}. \quad (\text{A21})$$

If we know uncertainties of parameters  $M_1, P_1$ , and  $P'$  ( $\delta M_1, \delta P_1$ , and  $\delta P'$ ) we can simply compute the uncertainty of prediction of the time of the phase function  $\vartheta, t(\vartheta)$  (eq A14), the predicted phase function  $\delta\vartheta(t)$  (eq A19) and the uncertainty of the instantaneous period estimate  $\delta P(t)$  (eq A20)

$$\begin{aligned} \delta\Theta(\vartheta) &= \sqrt{(\delta M_1)^2 + [\delta P_1(\vartheta - \eta_1)]^2 + \left[\frac{P_1\delta P'(\vartheta - \eta_2)(\vartheta - \eta_3)}{2}\right]^2}, \\ \delta P(t) &= \sqrt{(\delta P_1)^2 + \left[P_1\delta P' \left(\vartheta - \frac{\eta_{21}}{2}\right)\right]^2}; \quad \delta\vartheta(t) \simeq \frac{\delta\Theta(\vartheta)}{P_1}. \end{aligned} \quad (\text{A22})$$

Using the following relations we can easily return to Maclaurin ephemeris:

$$M_0 = M_1 - \eta_1 P_1 - \frac{P'P_1\eta_{20}}{2}, \quad P_0 = P_1 - \frac{P_1 P' \eta_{21}}{2}, \quad \dot{P} = P'. \quad (\text{A23})$$

If we put the origin of epochs near to  $M_1$ , so that  $\eta_1 = 0$ , a lot of relations become simpler:

$$\begin{aligned} \Theta(\vartheta) &\simeq M_1 + P_1(\vartheta) + \frac{P'P_1}{2}(\vartheta^2 - \eta_{21}\vartheta - \eta_{20}) = \\ &= M_1 + P_1(\vartheta) + \frac{P'P_1}{2}(\vartheta - \eta_2)(\vartheta - \eta_3), \quad \text{where} \end{aligned} \quad (\text{A24})$$

$$\eta_{21} = \frac{\overline{\vartheta^3}}{\overline{\vartheta^2}}; \quad \eta_{20} = \overline{\vartheta^2}; \quad \eta_{3,2} = \frac{\overline{\vartheta^3} \pm \sqrt{\overline{\vartheta^3}^2 + 4\overline{\vartheta^2}^3}}{2\overline{\vartheta^2}}, \quad (\text{A25})$$

$$P(\vartheta) = \frac{dt}{d\vartheta} = P_1 \left[1 + P' \left(\vartheta - \frac{\eta_{21}}{2}\right)\right]; \quad (\text{A26})$$

$$M_0 = M_1 - \frac{P'P_1\eta_{20}}{2}, \quad P_0 = P_1 - \frac{P_1 P' \eta_{21}}{2}, \quad (\text{A27})$$

$$\vartheta_1 = \frac{t - M_1}{P_1}; \quad \vartheta(\vartheta_1) = \vartheta_1 - \frac{P'}{2}(\vartheta_1^2 - \eta_{21}\vartheta_1 - \eta_{20}), \quad (\text{A28})$$

$$P(t) = P_1 \frac{d\vartheta_1}{d\vartheta} \simeq P_1 \left[1 + P' \left(\vartheta_1 - \frac{\eta_{21}}{2}\right)\right]; \quad \dot{P}(t) = P'. \quad (\text{A29})$$

**Table A1.** Coefficients  $\beta_{ij}$  of the asymmetrical part of the light curve model harmonic polynomial till  $m = 11$ -th order.

$i$	$\beta_{i1}$	$\beta_{i2}$	$\beta_{i3}$	$\beta_{i4}$	$\beta_{i5}$	$\beta_{i6}$	$\beta_{i7}$
2	0.8944	-0.4472	0	0	0	0	0
3	0.3586	0.7171	-0.5976	0	0	0	0
4	0.1952	0.3904	0.5855	-0.6831	0	0	0
5	0.1231	0.2462	0.3693	0.4924	-0.7385	0	0
6	0.0848	0.1696	0.2544	0.3392	0.4241	-0.7774	0
7	0.0620	0.1240	0.1861	0.2481	0.3101	0.3721	-0.8062
8	0.0473	0.0947	0.1420	0.1894	0.2367	0.2840	0.3314
9	0.0373	0.0747	0.1120	0.1493	0.1866	0.2240	0.2613
10	0.0302	0.0604	0.0906	0.1208	0.1509	0.1811	0.2113
11	0.0249	0.0498	0.0748	0.0997	0.1246	0.1495	0.1745

$i$	$\beta_{i8}$	$\beta_{i9}$	$\beta_{i10}$	$\beta_{i11}$
2 ÷ 7	0	0	0	0
8	-0.8284	0	0	0
9	0.2986	-0.8460	0	0
10	0.2415	0.2717	-0.8604	0
11	0.1994	0.2243	0.2492	-0.8723

#### A4 Modelling light curves of chemically peculiar stars

The observed light curves of chemically peculiar stars can be easily described as strictly periodic harmonic polynomials of the order  $m = 2 \div 18$  with a period of 0.5 to several hundred days, corresponding to the rotation periods of studied CP stars. The underlying light curves sometimes needed to be expressed by a harmonic polynomial of about tenth order, typical of mCP stars with the complicated appearance of surface photometric spots and semi-transparent structures trapped in co-rotating stellar magnetospheres.

##### A4.1 Monochromatic light curves

For an explicit description of a monochromatic light curve with the effective wavelength  $\lambda$ , it is advantageous to use special harmonic polynomials (SHP). SHP of the  $m$ -th order,  $\Xi(\vartheta, m) = [\Xi_1, \Xi_2, \dots, \Xi_{2m-1}]$ , is a row vector with the length  $2m-1$ , which represent a base of mutually orthonormal harmonic functions with zero time derivative at the phase  $\varphi = 0$ , while  $\mathbf{b}(\lambda) = [b_1, b_2, \dots, b_{2m-1}]'$  parameters.  $m$  of them are simple symmetric functions with an extreme at phase 0, and  $(m-1)$  are antisymmetric functions with zero derivatives at phase 0. Such polynomials have one of their extremes in the phase  $\varphi = 0$ :

$$\begin{aligned} \Xi_1(\vartheta, m) &= \cos(2\pi\vartheta); & \Xi_{2i-2}(\vartheta, m) &= \cos(2\pi i\vartheta); \\ \Xi_{2i-1}(\vartheta, m) &= \sum_{j=1}^i \beta_{ij} \sin(2\pi j\vartheta); & i &= 2, 3, \dots, m; \end{aligned} \quad (\text{A30})$$

when the coefficients  $\beta_{ij}$  (given in Table A1) fulfils the following constraints

$$\sum_{j=1}^i j \beta_{ij}(\lambda) = 0; \quad \sum_{j=1}^i \beta_{ij} \beta_{kj} = \delta_{ik}; \quad i \geq k. \quad (\text{A31})$$

Parameters  $\beta_{ij}$  that fulfill the orthonormalization constraints (Eq: A31) are in Table A1. The model of the monochromatic light curve  $F(\vartheta, m)$  then may be expressed in the form

$$F(\vartheta, m) = m_k + \Xi(\vartheta, m) \cdot \mathbf{b}(\lambda) = m_k + \sum_{i=1}^{2m-1} b_i(\lambda) \Xi_i(\vartheta, m), \quad (\text{A32})$$

where  $m_k$  are the mean magnitudes of observational subsets. In the case of HD 34736 we have divided observations into eight segments – see Table 2.

A robust measure of monochromatic variability of a periodic light curve is the so-called *effective amplitude*  $A_{\text{eff}}(\lambda)$ , which can be easily expressed thanks to the orthonormality of the basis of special harmonic polynomials:

$$A_{\text{eff}}(\lambda) = 2 \text{norm}(\mathbf{b}(\lambda)) = 2 \sqrt{\sum_{i=1}^{2m-1} b_i^2(\lambda)}. \quad (\text{A33})$$

#### APPENDIX B: LIGHT-TRAVEL TIME DELAY

The orbital motion of the stars in the binary affects the photometric behavior of the system. The light-travel time (Roemer) delay applies in the variability of the individual components; with a suitable inclination of the orbit, mutual eclipses of binary members can also occur. Since we know the parameters of the spectroscopic path with extraordinary precision, we can (see Table 4) reliably calculate and predict the mentioned effects.

Following the table, it will assume that the orbital period (the time between two consecutive passages through the same anomaly) is  $P_{\text{orb}} = 83^{\text{d}}219(3)$ ; the numerical eccentricity is  $e = 0.8103(3)$ , the fundamental moment of the periastron passage is  $T_p = 2457415.346(3)$ ; the projections of the semiaxes of the individual components in light days are:  $A_A = a_A \sin i = 0.00183 \text{ ld}$ ;  $A_B = a_B \sin i = 0.00256 \text{ ld}$  ( $i$  being the unknown inclination angle of the orbit), and the argument of the periastron (the angle from the orbital ascending node to its periastron, measured in the direction of motion), in radians:  $\omega = 1.470(2) \text{ rad}$ . Using these parameters we can compute for any time  $t$  the following quantities: a true anomaly  $\theta$ ,  $E$  an eccentric anomaly, and  $M$  a mean anomaly.

$$E(M) = M + e \sin E; \quad \text{where } M(t) = 2\pi \frac{t - T_p}{P_{\text{orb}}}; \quad (\text{B1})$$

$$\theta(E) = 2 \arctan \left[ \sqrt{\frac{1+e}{1-e}} \tan \left( \frac{E}{2} \right) \right] + 2\pi \text{round} \left( \frac{E}{2\pi} \right); \quad (\text{B2})$$

$$E(\theta) = 2 \arctan \left[ \sqrt{\frac{1-e}{1+e}} \tan \left( \frac{\theta}{2} \right) \right] + 2\pi \text{round} \left( \frac{\theta}{2\pi} \right). \quad (\text{B3})$$

Suppose we want to clean the timing of the events on the individual components of the double stars from their orbital motion. In that case, we can do it by offsetting the time corrections of the light-travel time delay (Borkovits et al. 2016)  $\Delta_A(t)$  and  $\Delta_B(t)$ , where  $t_A$  and  $t_B$  are the times related to the gravity center of the system.

$$\Delta_A(t) = A_A \frac{(1-e^2) \sin[\theta(t) + \omega]}{1 + e \cos \theta}; \quad t_A = t - \Delta_A(t); \quad (\text{B4})$$

$$\Delta_B(t) = -A_B \frac{(1-e^2) \sin[\theta(t) + \omega]}{1 + e \cos \theta}; \quad t_B = t - \Delta_B(t).$$

The above relations for specific values of its eccentricity and argument of periastron show the binary's components spend most of their time near the apastron, with component A being on average seven light minutes closer to us than the less massive and smaller component B (see Fig. B1).

If, on the other hand, we want to know the prediction of the time of some significant moment from the observer's point of view (e.g. time of maximum  $\theta(E)$ ) for the epoch  $E$ , the moment of the prediction relative to the center of gravity of the system must be corrected by the corresponding LTT delay:

$$t_{\text{maxA}} = \theta(E_A) + \Delta_A(\theta(E_A)), \quad t_{\text{maxB}} = \theta(E_B) + \Delta_B(\theta(E_B)). \quad (\text{B5})$$

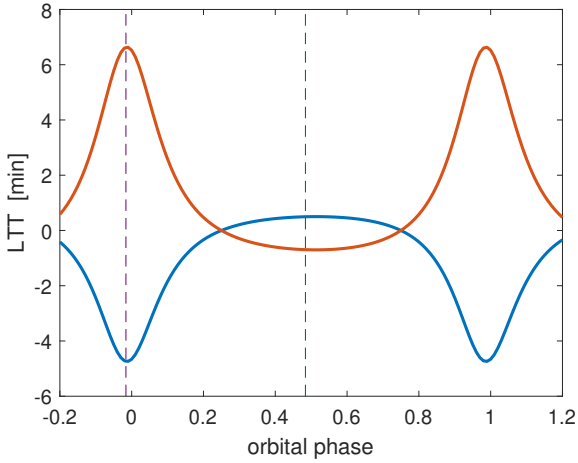


**Figure B1.** The dependence of light-travel time delay on the orbital phase as introduced by (13) for A (blue line) and B (red line) components. The green dashed line signs the phase of the periastron passage, while the magenta line signs the apastron passage.

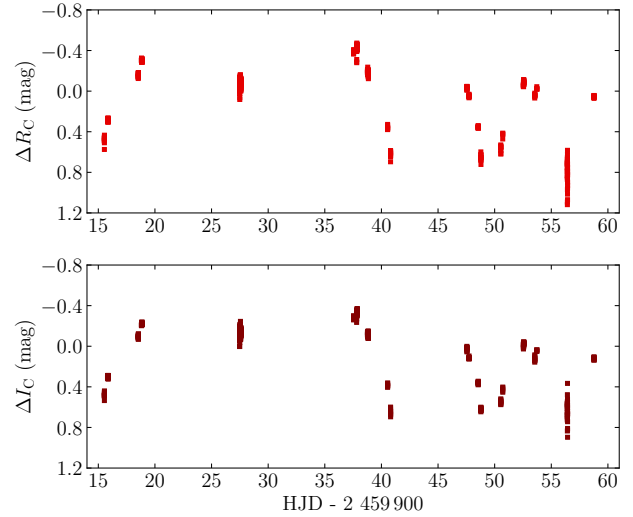


**Figure C2.** Light variation of UCAC4 414-008437 in filters  $R_C$  and  $I_C$  registered with the DK154 telescope at La Silla Observatory.

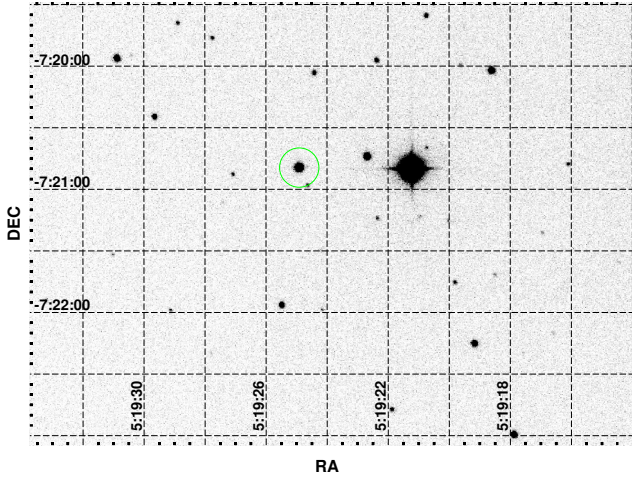


**Figure C1.** Field of view of the DK154 telescope with the brightest star HD 34736 and the star UCAC4 414-008437 (green circle) located at an apparent distance  $54.83''$  corresponding to about 2.5 pixels of the detector of the *TESS* satellite.

### APPENDIX C: ELIMINATION OF UCAC4 414-008437 LIGHT VARIATION

Our follow-up photometry of a young red pre-main-sequence star UCAC4 414-008437 separated by 2.5 *TESS* pixels from HD 34736 (Fig. C1) shows that its light curve remains relatively smooth on the timescale of weeks (Fig. C2). This fact makes it possible to identify this star as a source of an additional signal in the *TESS* data (Sec. 3.1.1) and correct these light curves for the contribution of specific UCAC4 414-008437 variations, assuming that all aperiodic variations (Fig. C3) longer than 0.1 days are caused solely by this object.

The relevance and accuracy of this correction, which decreases the scatter of the fit to 0.32 mmag, was independently confirmed by a custom treatment of the original *TESS* data using a smaller numerical aperture lowering several times the contribution of the parasitic light from the third component. We found that the corrected light curves

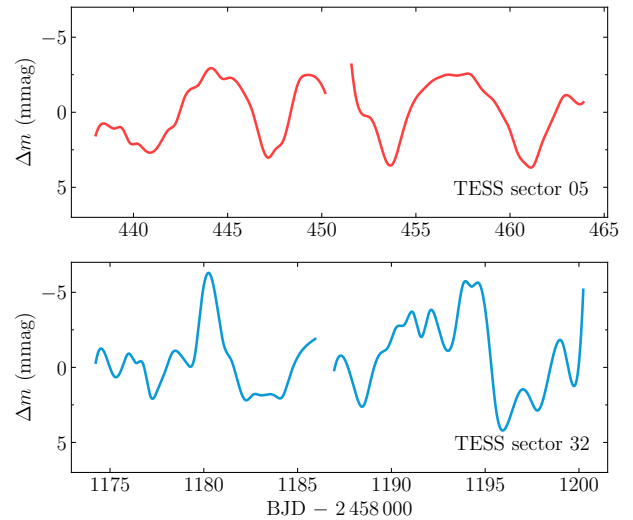


**Figure C3.** The third component *TESS* light curve contribution in mmags for Sectors 05 and 32.

obtained by both methods agree very well, but we opted for the first one as it is a bit more accurate.



## ONLINE MATERIAL

Table 1: Summary table with individual measurements and corresponding errors. Heliocentric Julian Date (HJD) is given for the middle of exposures. The second column contains the name of the used instrument. The longitudinal magnetic field  $\langle B_z \rangle$  of the primary component and the method of its evaluation are in the third and fourth columns. The radial velocity of components A and B measured from the LSD profiles or from the modelling of Mg II 448.1 nm line are given as  $V_r(A)$  and  $V_r(B)$  with corresponding subscripts. By three asterisks in the sixth column, we marked the spectra averaged within the nights grouped by blank lines. The last three columns contain quadratic rotational phases  $\vartheta_A$  and  $\vartheta_B$ , and the orbital phase  $\varphi_{\text{orb}}$ . The full table is available online.

HJD 2450000+	Instrument	$\langle B_z \rangle$ (G)	Method	$V_r(A)_{\text{LSD}}$ (km s <sup>-1</sup> )	$V_r(B)_{\text{MgII}}$ ( $\pm 20$ km s <sup>-1</sup> )	$V_r(B)_{\text{LSD}}$ (km s <sup>-1</sup> )	$\vartheta_A$	$\vartheta_B$	$\varphi_{\text{orb}}$
6589.4929	MSS	-3500 440	COG	-30.39 0.95	-	-	0.426	0.206	0.560
6639.4980	MSS	-160 530	COG	40.14 0.50	-30	-	0.496	0.867	0.161
6644.4389	MSS	-4580 560	COG	41.79 0.85	-5	-	0.356	0.320	0.220
6732.1696	MSS	3650 360	COG	46.35 0.65	***	-	0.899	0.162	0.275
6732.1855	MSS	3841 340	COG	47.98 0.61	***	-	0.911	0.192	0.275
6732.2008	MSS	4338 270	COG	47.58 0.60	***	-	0.923	0.222	0.275
6732.2154	MSS	4600 360	COG	46.85 0.56	-20	-	0.935	0.250	0.275
6732.2313	MSS	4250 300	COG	46.53 0.53	***	-	0.947	0.280	0.275
6732.2452	MSS	5170 340	COG	45.88 0.54	***	-	0.958	0.307	0.275
6732.2605	MSS	4100 430	COG	44.67 0.49	***	-	0.970	0.336	0.276
6739.1905	MSS	-3280 550	COG	56.19 0.43	***	-	0.384	0.596	0.359
6739.2058	MSS	-3000 340	COG	59.16 0.46	***	-	0.396	0.625	0.359
6739.2204	MSS	-4690 570	COG	60.42 0.46	-60	-	0.407	0.653	0.359
6739.2356	MSS	-4590 550	COG	62.10 0.46	***	-	0.419	0.682	0.359
6739.2509	MSS	-3590 500	COG	63.00 0.46	***	-	0.431	0.712	0.360
6740.1876	MSS	-3400 630	COG	57.67 0.41	***	-	0.163	0.504	0.371
6740.2022	MSS	-3440 590	COG	59.67 0.44	***	-	0.174	0.532	0.371
6740.2175	MSS	-4400 450	COG	58.78 0.47	-67	-	0.186	0.561	0.371
6740.2328	MSS	-3400 570	COG	58.98 0.47	***	-	0.198	0.591	0.371
6740.2473	MSS	-4300 520	COG	61.16 0.48	***	-	0.209	0.618	0.372
6939.5133	MSS	4330 1000	COG	-8.72 1.25	-	-	0.894	0.839	0.766
6939.5551	MSS	4250 930	COG	-1.52 1.13	-	-	0.927	0.919	0.767
6939.5849	MSS	4360 990	COG	4.89 1.09	-	-	0.950	0.976	0.767
6939.6002	MSS	3660 690	COG	6.04 1.02	-	-	0.962	0.006	0.767
6940.4503	MSS	2170 480	COG	9.83 0.54	***	-	0.626	0.632	0.777
6940.4655	MSS	1760 900	COG	9.93 0.54	***	-	0.638	0.661	0.778
6940.4815	MSS	3070 670	COG	9.64 0.52	***	-	0.651	0.691	0.778
6940.4967	MSS	2320 820	COG	9.59 0.55	***	-	0.663	0.721	0.778
6940.5183	MSS	960 740	COG	8.73 0.56	65	-	0.679	0.762	0.778
6940.5336	MSS	1980 810	COG	8.31 0.59	***	-	0.691	0.791	0.778
6940.5489	MSS	2400 800	COG	6.88 0.56	***	-	0.703	0.820	0.779
6940.5641	MSS	1750 850	COG	6.95 0.62	***	-	0.715	0.849	0.779
6940.5808	MSS	3020 1150	COG	6.49 0.60	***	-	0.728	0.881	0.779
6940.6051	MSS	1160 980	COG	10.69 1.54	***	-	0.747	0.928	0.779
6966.5068	MSS	4160 370	COG	26.46 0.51	***	-	0.984	0.480	0.090
6966.5221	MSS	3540 540	COG	28.22 0.48	***	-	0.996	0.510	0.091
6966.5381	MSS	3790 590	COG	29.33 0.46	***	-	0.009	0.540	0.091
6966.5554	MSS	3550 390	COG	30.65 0.47	0	-	0.022	0.573	0.091
6966.5707	MSS	2630 650	COG	32.15 0.45	***	-	0.034	0.603	0.091
6966.5874	MSS	3780 900	COG	33.04 0.44	***	-	0.047	0.635	0.091
6966.6026	MSS	2670 770	COG	34.29 0.42	***	-	0.059	0.664	0.092

Continued on next page

Table 1 – continued from previous page

HJD 2450000+	Instrument	$\langle B_z \rangle$ (G)	Method	$V_r(A)_{\text{LSD}}$ (km s <sup>-1</sup> )	$V_r(B)_{\text{MgII}}$ ( $\pm 20$ km s <sup>-1</sup> )	$V_r(B)_{\text{LSD}}$ (km s <sup>-1</sup> )	$\vartheta_A$	$\vartheta_B$	$\varphi_{\text{orb}}$
6966.6179	MSS	3050 660	COG	34.84 0.45	***	–	0.071	0.693	0.092
6967.4062	MSS	3680 650	COG	35.65 0.57	***	–	0.687	0.201	0.101
6967.4207	MSS	2650 610	COG	35.01 0.56	***	–	0.698	0.229	0.101
6967.4367	MSS	4040 790	COG	33.20 0.61	***	–	0.711	0.259	0.102
6967.4527	MSS	3200 830	COG	32.76 0.61	***	–	0.723	0.290	0.102
6967.4694	MSS	2540 480	COG	31.34 0.58	***	–	0.736	0.322	0.102
6967.4853	MSS	2800 510	COG	29.34 0.55	***	–	0.749	0.352	0.102
6967.5006	MSS	2050 430	COG	27.32 0.56	***	–	0.761	0.382	0.102
6967.5159	MSS	2590 580	COG	25.90 0.56	–5	–	0.773	0.411	0.103
6967.5332	MSS	2150 540	COG	23.42 0.58	***	–	0.786	0.444	0.103
6967.5485	MSS	3000 640	COG	21.49 0.61	***	–	0.798	0.473	0.103
6967.5638	MSS	3400 480	COG	21.51 0.60	***	–	0.810	0.503	0.103
6967.5798	MSS	3080 600	COG	22.26 0.63	***	–	0.822	0.533	0.103
6967.5917	MSS	3020 640	COG	21.13 0.59	***	–	0.832	0.556	0.103
6967.6124	MSS	2400 490	COG	21.28 0.59	***	–	0.848	0.596	0.104
6967.6248	MSS	3630 660	COG	21.18 0.61	***	–	0.858	0.619	0.104
6968.6215	MSS	2120 770	COG	42.60 1.61	–	–	0.636	0.526	0.116
6969.6202	MSS	–3000 1100	COG	37.71 1.32	–	–	0.417	0.437	0.128
6970.3813	MSS	2000 850	COG	36.35 1.04	***	–	0.011	0.893	0.137
6970.4077	MSS	1520 640	COG	34.41 0.40	***	–	0.032	0.944	0.137
6970.4230	MSS	1760 800	COG	35.75 0.41	***	–	0.044	0.973	0.137
6970.4382	MSS	1340 820	COG	37.48 0.45	***	–	0.056	0.002	0.138
6970.4535	MSS	1940 600	COG	40.00 0.40	***	–	0.068	0.031	0.138
6970.4778	MSS	270 770	COG	40.58 0.41	***	–	0.087	0.078	0.138
6970.4931	MSS	–220 970	COG	41.55 0.40	***	–	0.098	0.107	0.138
6970.5084	MSS	–750 770	COG	41.48 0.41	–10	–	0.110	0.136	0.139
6970.5230	MSS	–540 790	COG	40.22 0.41	***	–	0.122	0.164	0.139
6970.5383	MSS	–710 820	COG	39.46 0.39	***	–	0.134	0.194	0.139
6970.5528	MSS	–1100 740	COG	38.35 0.39	***	–	0.145	0.221	0.139
6970.5681	MSS	–1730 650	COG	37.64 0.37	***	–	0.157	0.251	0.139
6970.5834	MSS	–3880 800	COG	36.90 0.38	***	–	0.169	0.280	0.139
6970.5980	MSS	–3110 880	COG	36.24 0.36	***	–	0.180	0.308	0.140
6972.3932	MSS	–700 725	COG	39.22 0.46	***	–	0.583	0.742	0.161
6972.4085	MSS	1160 550	COG	40.16 0.47	***	–	0.595	0.772	0.161
6972.4231	MSS	2100 530	COG	39.37 0.49	***	–	0.606	0.800	0.162
6972.4383	MSS	2420 700	COG	40.15 0.49	***	–	0.618	0.829	0.162
6972.4529	MSS	1650 660	COG	40.32 0.51	–20	–	0.630	0.857	0.162
6972.4682	MSS	2840 980	COG	40.53 0.51	***	–	0.642	0.886	0.162
6972.4828	MSS	2360 880	COG	39.44 0.51	***	–	0.653	0.914	0.162
6972.5476	MSS	2140 580	COG	41.18 0.54	***	–	0.704	0.038	0.163
6973.3453	MSS	–4790 670	COG	37.84 0.39	***	–	0.327	0.564	0.173
6973.3599	MSS	–4670 650	COG	38.87 0.41	***	–	0.338	0.592	0.173
6973.3752	MSS	–3860 630	COG	38.67 0.37	***	–	0.350	0.621	0.173
6973.3898	MSS	–3600 830	COG	39.07 0.44	***	–	0.362	0.649	0.173
6973.4050	MSS	–3640 690	COG	38.65 0.44	–20	–	0.373	0.678	0.173
6973.4196	MSS	–4430 610	COG	39.40 0.45	***	–	0.385	0.706	0.174
6973.4349	MSS	–4360 460	COG	38.48 0.43	***	–	0.397	0.735	0.174
6973.4495	MSS	–2950 590	COG	38.78 0.47	***	–	0.408	0.763	0.174
6973.4648	MSS	–2090 520	COG	38.25 0.44	***	–	0.420	0.793	0.174
6973.4794	MSS	–2240 490	COG	39.33 0.46	***	–	0.432	0.821	0.174
6973.4981	MSS	–3040 780	COG	40.12 1.26	***	–	0.446	0.856	0.174

Continued on next page

Table 1 – continued from previous page

HJD 2450000+	Instrument	$\langle B_z \rangle$ (G)	Method	$V_r(A)_{\text{LSD}}$ (km s <sup>-1</sup> )	$V_r(B)_{\text{MgII}}$ ( $\pm 20$ km s <sup>-1</sup> )	$V_r(B)_{\text{LSD}}$ (km s <sup>-1</sup> )	$\vartheta_A$	$\vartheta_B$	$\varphi_{\text{orb}}$
6973.5134	MSS	-2300 1180	COG	40.08 1.26	***	–	0.458	0.886	0.175
6973.5287	MSS	-2200 660	COG	40.10 1.25	***	–	0.470	0.915	0.175
6973.5432	MSS	-400 1000	COG	40.94 1.24	***	–	0.481	0.943	0.175
6973.5585	MSS	-680 550	COG	40.39 1.19	***	–	0.493	0.972	0.175
6993.5633	MSS	890 920	COG	84.28 0.92	–	–	0.121	0.250	0.416
6995.3952	MSS	770 760	COG	94.03 1.09	***	***	0.552	0.755	0.438
6995.4119	MSS	1540 1000	COG	94.69 0.91	***	***	0.565	0.787	0.438
6995.4279	MSS	840 920	COG	95.29 1.10	-20	-88.6 7.7	0.578	0.818	0.438
6995.4438	MSS	2920 720	COG	95.25 1.14	***	***	0.590	0.848	0.438
6995.4591	MSS	3920 970	COG	95.98 1.02	***	***	0.602	0.878	0.438
6995.4924	MSS	2030 1080	COG	102.41 1.59	***	***	0.628	0.941	0.439
6995.5077	MSS	1200 1200	COG	102.14 1.56	***	***	0.640	0.971	0.439
6995.5237	MSS	2870 760	COG	103.12 1.53	***	***	0.652	0.001	0.439
7085.1727	MSS	2510 520	COG	-41.91 1.44	***	***	0.693	0.514	0.516
7085.1949	MSS	2700 330	COG	-44.80 1.42	***	***	0.711	0.556	0.517
7085.2172	MSS	2555 395	COG	-48.32 1.43	95	111.9 6.3	0.728	0.599	0.517
7085.2394	MSS	3230 635	COG	-50.32 1.36	***	***	0.745	0.641	0.517
7090.2264	MSS	2610 490	COG	-12.64 0.57	***	–	0.642	0.180	0.577
7090.2452	MSS	2700 300	COG	-16.01 0.58	***	–	0.657	0.216	0.577
7090.2605	MSS	2870 540	COG	-18.74 0.59	80	–	0.669	0.245	0.578
7090.2778	MSS	2500 500	COG	-21.27 0.59	***	–	0.683	0.278	0.578
7090.2931	MSS	2220 370	COG	-21.36 0.60	***	–	0.695	0.307	0.578
7091.1757	MSS	-3660 500	COG	-17.28 0.38	***	–	0.384	0.996	0.589
7091.1930	MSS	-3850 430	COG	-20.46 0.38	***	–	0.398	0.029	0.589
7091.2090	MSS	-3850 620	COG	-21.64 0.38	***	–	0.410	0.059	0.589
7091.2243	MSS	-2640 600	COG	-22.07 0.40	***	–	0.422	0.089	0.589
7091.2396	MSS	-3530 540	COG	-21.77 0.42	90	–	0.434	0.118	0.589
7091.2562	MSS	-2480 840	COG	-21.84 0.43	***	–	0.447	0.150	0.589
7091.2715	MSS	-1800 630	COG	-21.88 0.43	***	–	0.459	0.179	0.590
7091.2868	MSS	-1920 630	COG	-22.09 0.45	***	–	0.471	0.208	0.590
7092.1770	MSS	-2560 390	COG	-18.72 0.40	***	–	0.167	0.911	0.601
7092.1943	MSS	-3130 610	COG	-17.16 0.40	***	–	0.180	0.944	0.601
7092.2353	MSS	-3450 510	COG	-16.30 0.38	90	–	0.212	0.022	0.601
7092.2506	MSS	-4000 500	COG	-17.02 0.39	***	–	0.224	0.052	0.601
7092.2652	MSS	-4850 550	COG	-17.47 0.37	***	–	0.236	0.080	0.602
7092.2818	MSS	-4470 430	COG	-17.38 0.37	***	–	0.248	0.111	0.602
7331.4324	MSS	–	–	88.12 0.70	-76	–	0.090	0.646	0.476
7332.5339	MSS	3500 520	COG	-1.07 0.43	95	–	0.951	0.754	0.489
7414.2401	MSS	3180 380	COG	95.17 1.82	***	***	0.786	0.070	0.471
7414.2623	MSS	3550 740	COG	92.24 1.86	***	***	0.803	0.112	0.471
7414.2998	MSS	4240 450	COG	83.89 1.04	***	***	0.833	0.184	0.471
7414.3214	MSS	4720 580	COG	82.74 1.18	-80	-107.8 8.6	0.849	0.225	0.472
7414.3540	MSS	3530 550	COG	81.76 1.11	***	***	0.875	0.287	0.472
8178.2653	MSS	1510 680	COG	-10.43 0.35	65	–	0.693	0.765	0.651
8178.2799	MSS	2360 670	COG	-10.92 0.36	***	–	0.704	0.793	0.652
9211.3463	MSS	3360 570	COG	22.19 0.95	–	–	0.780	0.223	0.065

Continued on next page

Table 1 – continued from previous page

HJD 2450000+	Instrument	$\langle B_z \rangle$ (G)	Method	$V_r(A)_{\text{LSD}}$ (km s <sup>-1</sup> )	$V_r(B)_{\text{MgII}}$ ( $\pm 20$ km s <sup>-1</sup> )	$V_r(B)_{\text{LSD}}$ (km s <sup>-1</sup> )	$\vartheta_A$	$\vartheta_B$	$\varphi_{\text{orb}}$
9213.3581	MSS	-5930 480	COG	28.18 0.73	–	–	0.352	0.072	0.090
6972.1470	ESPaDOnS	-4020 96	LSD	34.66 0.21	0	–	0.391	0.271	0.158
7013.0363	ESPaDOnS	-4905 98	LSD	-10.46 0.17	88	–	0.336	0.502	0.650
7021.0463	ESPaDOnS	1958 99	LSD	4.44 0.21	35	–	0.594	0.824	0.746
7021.9910	ESPaDOnS	-5158 77	LSD	1.20 0.16	45	–	0.333	0.631	0.757
7030.0351	ESPaDOnS	2403 108	LSD	17.39 0.21	30	–	0.618	0.020	0.854
7031.0379	ESPaDOnS	-3517 104	LSD	9.77 0.22	26	–	0.401	0.938	0.866
7032.0343	ESPaDOnS	-4858 81	LSD	13.11 0.17	25	–	0.180	0.844	0.878
7033.0303	ESPaDOnS	4054 109	LSD	8.43 0.29	20	–	0.958	0.750	0.890
7034.0247	ESPaDOnS	3371 81	LSD	17.04 0.20	13	–	0.735	0.652	0.902
7035.0138	ESPaDOnS	-174 115	LSD	19.46 0.25	37	–	0.508	0.544	0.914
7405.9464	ESPaDOnS	-5158 96	LSD	65.32 0.17	-55	-59.4 4.4	0.308	0.198	0.371
7406.8023	ESPaDOnS	3622 120	LSD	64.35 0.24	–	–	0.976	0.836	0.381
7413.7178	ESPaDOnS	-4572 123	LSD	96.76 0.19	-70	-60.7 4.3	0.378	0.070	0.464
7413.9017	ESPaDOnS	365 131	LSD	102.02 0.20	-70	-89.3 2.9	0.522	0.422	0.467
7414.7185	ESPaDOnS	-4543 99	LSD	79.92 0.15	-40	-48.0 3.6	0.160	0.985	0.476
7414.8326	ESPaDOnS	-5632 88	LSD	73.13 0.17	-50	-64.5 3.9	0.249	0.203	0.478
7414.9724	ESPaDOnS	-4632 109	LSD	63.44 0.17	-40	-48.5 4.4	0.358	0.471	0.479
7415.7189	ESPaDOnS	3996 110	LSD	0.42 0.28	60	–	0.941	0.899	0.488
7415.8335	ESPaDOnS	1202 116	LSD	-1.22 0.24	65	–	0.031	0.118	0.490
7415.9739	ESPaDOnS	-3798 105	LSD	-7.39 0.20	65	–	0.140	0.387	0.491
7416.7190	ESPaDOnS	3945 97	LSD	-30.27 0.23	72	–	0.723	0.812	0.500
7416.9011	ESPaDOnS	5010 105	LSD	-44.10 0.22	105	123.2 3.7	0.865	0.160	0.503
6972.9243	dimaPol	4310 796	Pol	–	–	–	0.998	0.759	0.168
6973.9366	dimaPol	5429 438	Pol	–	–	–	0.789	0.695	0.180
6974.9273	dimaPol	3012 380	Pol	–	–	–	0.563	0.591	0.192
6975.9563	dimaPol	-5266 473	Pol	–	–	–	0.367	0.560	0.204
6991.8906	dimaPol	3512 448	Pol	–	–	–	0.815	0.049	0.395
6992.8882	dimaPol	2617 269	Pol	–	–	–	0.594	0.958	0.407
6994.9034	dimaPol	-4446 651	Pol	–	–	–	0.168	0.814	0.432
7084.6555	dimaPol	-6850 475	Pol	–	–	–	0.289	0.525	0.510
7085.6545	dimaPol	1419 351	Pol	–	–	–	0.070	0.435	0.522
7088.6693	dimaPol	-3993 279	Pol	–	–	–	0.426	0.202	0.558
7330.6680	HERMES	–	–	103.44 0.51	-105	-78.7 4.9	0.493	0.183	0.466
7331.6653	HERMES	–	–	74.51 0.43	-60	–	0.272	0.092	0.478
7332.6568	HERMES	–	–	-5.65 0.38	85	–	0.047	0.989	0.490
7333.6613	HERMES	–	–	-44.59 0.55	124	–	0.832	0.910	0.502
7334.6584	HERMES	–	–	-33.35 0.27	84	–	0.611	0.817	0.514
7335.5781	HERMES	–	–	-44.35 0.46	–	–	0.330	0.576	0.525
7335.6840	HERMES	–	–	-41.51 0.65	–	–	0.412	0.779	0.527
7370.5438	HERMES	–	–	23.82 0.40	19	–	0.650	0.463	0.946
7413.3551	HERMES	–	–	104.55 0.45	-109	-70.8 4.0	0.095	0.376	0.460
7413.4886	HERMES	–	–	103.41 0.46	-90	–	0.199	0.631	0.462
7414.3730	HERMES	–	–	84.48 0.43	-70	-108.3 4.1	0.890	0.324	0.472
7414.4669	HERMES	–	–	86.76 0.46	-70	-92.7 4.3	0.963	0.504	0.473
7414.5563	HERMES	–	–	87.07 0.48	-50	-90.1 5.3	0.033	0.675	0.474
7415.3874	HERMES	–	–	38.90 0.30	0	–	0.682	0.265	0.484
7415.4866	HERMES	–	–	23.31 0.35	0	–	0.760	0.455	0.486
7416.3684	HERMES	–	–	-27.62 0.73	70	138.7 3.4	0.449	0.142	0.496
7417.0260	MRES	–	–	-41.08 0.19	100	132.4 6.7	0.963	0.399	0.504
9563.0630	MRES	–	–	57.6 0.8	–	-27.9 8.7	0.549	0.125	0.292
9564.1195	MRES	–	–	53.3 0.9	–	-8.7 6.2	0.375	0.146	0.305
9565.0816	MRES	–	–	58.5 0.5	–	-17.7 3.0	0.126	0.987	0.316